Human Histology

A MICROFICHE ATLAS

VOLUME TWO ORGANS AND SYSTEMS

Stanley L. Erlandsen and Jean E. Magney

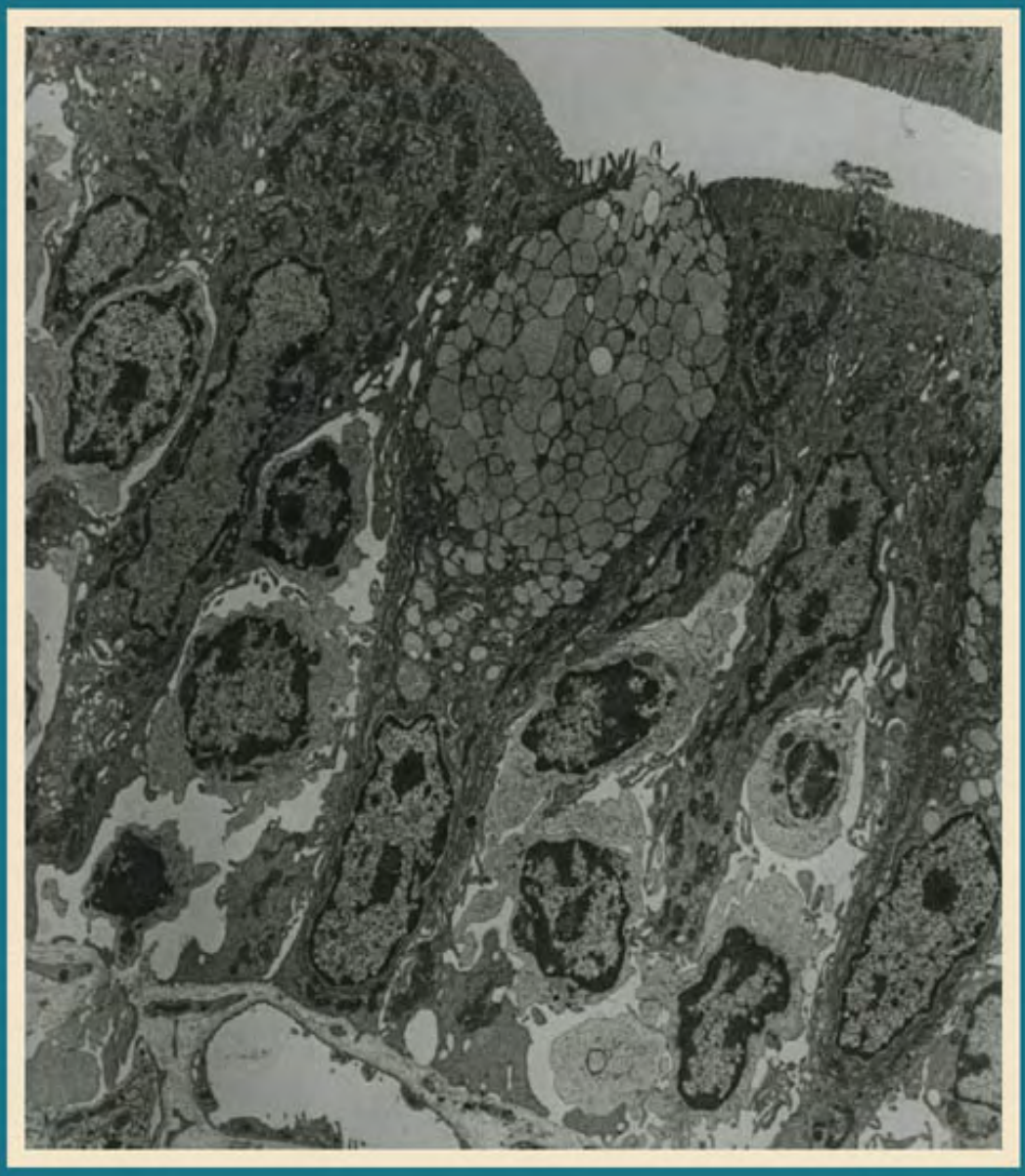

Human Histology

Volume 2

Publications in the Health Sciences

Publication of this book was assisted
by a McKnight Foundation grant to the
University of Minnesota Press's
program in the health sciences.

HUMAN HISTOLOGY
A Microfiche Atlas

Volume 2
ORGANS AND SYSTEMS

Stanley L. Erlandsen
and Jean E. Magney

University of Minnesota Press ☐ Minneapolis

Published by the University of Minnesota Press.
2037 University Avenue Southeast, Minneapolis MN 55414

Published simultaneously in Canada by Fitzhenry & Whiteside Limited, Markham.

Printed in the United States of America

Library of Congress Cataloging-in-Publication Data
Erlandsen, Stanley L.
Human Histology
(Publications in the health sciences)
Includes index.
Contents: v. 1. Cells and tissues—v. 2. Organs and systems.
1. Histology—Atlases. 2. Microfiches. I. Magney, Jean E. II. Title. III. Series. [DNLM: 1. Histology—atlases. 2. Histology—Microfiche. QS 17 E69h]
QM557.E75 1985 611'.018 85-8566
ISBN 0-8166-1385-0 (set)
ISBN 0-8166-1386-9 (v. 1)
ISBN 0-8166-1387-7 (v. 2)

The University of Minnesota is an equal-opportunity educator and employer.

To our spouses,
Betty Erlandsen and Robert Magney,
for their patience, understanding,
and unswerving support.

Contents

This page intentionally left blank

Preface

This microfiche atlas of human histology is designed to help students acquire a better understanding of histology and the dynamic activities of cells, tissues, and organs. Each volume stresses the interrelationships of light microscopic and ultrastructural features and illustrates structural-functional correlations by use of schematic diagrams. In addition to our own light and electron microscopic slide collection, we have utilized more than 300 micrographs from leading scientists as well as a number of excellent macrophotographs from Lennart Nilsson and micrographs from the cinephotomicroscopy of Dr. Richard Blandau.

To use this atlas in conjunction with any histology course, the student can consult the Contents or the Index to find individual images or groups of images. We have tried to enhance the student's understanding of the material by illustrating a specific structure in a number of different ways, so that adjacent frames show it as a drawing, light micrograph, electron micrograph, and so on. Adjacent frames may also present the same structure by light microscopy at low and high magnification to help orient the student and to serve as a transition to electron microscopy.

This atlas serves as a portable visual aid for the examination of cells, tissues, and organs outside the standard laboratory setting. To facilitate its use outside the classroom, the microfiche can be examined with any portable microfiche reader that has a 15X lens. The high quality of image reproduction in the microfiche has made it a valuable aid for group study when used with a microfiche projector. The WSI Informant II microfiche projector has been successfully used in the histology labs and the Biomedical Learning Center at the University of Minnesota; it has a removable lid that permits it to be used either as a portable microfiche reader or as a microfiche projector.

Five microfiche are included in Volume 1, nine in Volume 2. Each fiche contains 63 frames identified by rows (A) and columns (1-9). The text presents captions that are keyed to the fiche: fiche number (1-14) appears as a heading, and to the left of each caption are the letter and number of the frame described (A1, A2, A3, . . .; B1, B2, B3, . . .; and so on). Unless otherwise indicated, the captions describe cells, tissues, and organs that are either of human origin or from animals whose morphological features are indistinguishable from humans. A few abbreviations are used throughout the text:

EM	Electron Micrograph
FF	Freeze Fracture
H & E	Hematoxylin and Eosin Stain
LM	Light Micrograph
SEM	Scanning Electron Micrograph
TEM	Transmission Electron Micrograph

When abbreviations appear directly on an illustration, they are explained in the accompanying caption.

A 35 mm slide set covering the same material is also available through Minnesota Histographics, 2817 Aquila Avenue North, New Hope, MN 55427.

This microfiche atlas was developed for medical students at the University of Minnesota Medical School in response to their need for

an atlas that would correlate the structural information seen by modern light and electron microscopic techniques. We would like to acknowledge the contributions made by medical students at Minnesota who so enthusiastically used and studied the microfiche and made constructive comments to help us improve the atlas. We are grateful to the Educational Development Program and the Medical School administration at the University of Minnesota for their support. Most important, we wish to thank Dr. David W. Hamilton, Head of the Department of Anatomy, for his encouragement, enthusiastic support, and generosity in helping us complete this project. Numerous individuals, including more than 150 contributors of pictures, have also helped make the microfiche a successful tool for reviewing histology. In particular, we wish to thank: Cathy Sulik for her organizational skills in maintaining the histology slide collection; Chris Frethem for his assistance in electron microscopy and photographic reproduction; Walter Gutzmer for his photographic assistance; Jennifer Steinert for her careful typing of the Index; and Dr. Anna-Mary Carpenter for her development of the excellent histology slide collection at the University of Minnesota.

Human Histology

Volume 2

This page intentionally left blank

A1 Diagram of vessels comprising systemic circulation. Arterial vessels exhibit multiple layers of smooth muscle and relatively little connective tissue. On the other hand, veins are largely connective tissue with small amounts of smooth muscle. Notice that larger veins have longitudinally oriented bundles of smooth muscle in the tunica adventitia. TI, tunica intima; TM, tunica media; TA, tunica adventitia.

A2 Light micrograph (LM) showing full thickness of atrial wall. Easily distinguished are the three layers of the heart: the endocardium, the myocardium, and the epicardium, the last named containing a significant amount of fat. (Hematoxylin and eosin stain [H & E])

A3 Higher-magnification LM of atrial wall. Observe the thickened endocardium; note also the relatively large size of Purkinje fibers (lightly stained) in the subendocardial connective tissue as compared with the cardiac cells in the myocardium. (H & E)

A4 High-magnification LM of atrial wall showing presence of smooth muscle within endocardium. (H & E)

A5 Cross section of pectinate region of atrium as seen by LM. Cordlike arrangement of cardiac muscle cells projecting into the atrial lumen gives the endocardium an irregular appearance. Clots of red blood cells can be seen in the atrial lumen. (H & E)

A6 High-magnification LM of endocardium in pectinate region. Compare the thickness of the endocardium at this location with that seen in the smooth portion of the atrium in Frames A3 and A4. (H & E)

A7 High-magnification LM of epicardium. Note the presence of fat and large vessels in the subepicardial connective tissue. (H & E)

A8 Transmission electron micrograph (TEM) of atrial wall showing epicardium, underlying subepicardial connective tissue, and myocardium.

A9 High-magnification LM of subepicardial connective tissue showing presence of vessels and nerves, the latter containing parasympathetic ganglion cells. (H & E)

B1 TEM portraying cross-sectional profile of nodal (pacemaker) cell in atrioventricular node of mouse heart. Typical intercalated disks are absent in these cell types; however, junctional specializations between contiguous nodal cells do occur. Note the junction in the lower left-hand corner of this cell. The profile of this cell is delineated by short arrows directed toward the surface of the cell. N, nucleus; nu, nucleolus; a, nerve process with synaptic vesicles; o, Schwann cell invested nerve process; b, nerve bundle; g, Golgi complex; mv, multivesicular body; r, rough endoplasmic reticulum; f, fibroblast.

B2 Low-magnification LM of ventricular wall showing endocardium (right) and epicardium (left). Observe the thickness of the myocardium; (H & E)

B3 High-magnification LM of endocardial wall. The irregular surface of the endocardium is characteristic of the trabeculated region of the ventricle. (H & E)

B4 TEM of endocardium in ventricle. Connective tissue is found in both subendothelial layer and subendocardial layer.

B5 LM of ventricular wall. Purkinje fibers can be seen in the subendocardial connective tissue. Compare their size and staining characteristics with those of underlying cardiac cells in myocardium. (H & E)

B6 Diagram depicting skeleton of heart. Cardiac muscle cells attach to this connective tissue framework. The annuli ring each valve and are connected by the fibrous trigones. The membranous septum is part of the interventricular septum. The Purkinje, or conduction, system of the heart pierces the skeleton and descends into the interventricular septum.

B7 Macrophotograph of right ventricle illustrating papillary muscles and chordae tendineae attached to tricuspid valve.

B8 Low-power LM of heart wall in region of atrioventricular valve. Top of section shows the epicardium underlayed by a substantial amount of fat in which lies enbedded a branch of the coronary artery. At bottom, from left to right, can be seen the smooth surface, or sinus venarum portion, of the atrium, the atrioventricular valve, and the irregular, or roughened, surface of the trabeculae carneae. Locate the origin of the valve from the cardiac skeleton. (H & E)

B9 Low-power LM of semilunar valves. Observe the attachment of the valve, as well as the wall of the aorta, to the skeleton of the heart. (H & E)

C1 LM of aorta illustrating tunica intima, tunica media, and tunica adventitia. See A1. (H & E)

C2 Cross section of aorta as seen with Verhoeff stain. Note the distribution of elastin within the aortic wall.

C3 High-magnification LM of tunica intima and tunica media of aorta. Observe the distribution of connective tissue within these layers. (H & E)

C4 LM of tunica media and tunica adventitia of aorta. Small vessels, the vasa vasorum, can be seen within adventitia and tunica media. (H & E)

C5 LM of muscular artery illustrating tunica intima, tunica media, and tunica adventitia. See A1. (H & E)

C6 LM of muscular artery stained with Verhoeff technique. Note the distribution of elastin within the vessel wall; also small bundles of nerve can be seen in the surrounding connective tissue.

C7 LM of muscular artery stained by azan method. Note the distribution of collagen within the vessel wall.

C8 Higher-magnification LM of wall of muscular artery. Observe the well-defined internal elastic lamina and the presence of elastin fibers within the tunica media and tunica adventitia. (H & E)

C9 Higher-magnification LM of tunica intima. Notice the scalloped appearance of the internal elastic lamina. The tunica intima can be seen to consist of endothelial cells, a small amount of subendothelial connective tissue, and the bordering internal elastic lamina. (H & E)

D1 LM of cross section of muscular artery stained with Verhoeff method. Observe the distribution of elastin within the walls of the vessel and compare with that seen in C8.

D2 TEM of wall of muscular artery. Portions of the tunica media and the tunica intima are seen. Compare the distribution of elastin as seen by TEM to that seen by the Verhoeff method in D1. mej, myoendothelial junction.

D3 High-magnification LM of small arteriole in connective tissue in cross section. See A1. Observe the endothelial cell nuclei cut in cross section and the longitudinal section of the smooth muscle cells in the tunica media. (H & E)

D4 Electron micrograph of small arteriole. Compare the morphology of this arteriole at the ultrastructural level with that seen by light microscopy in D3.

D5 Electron micrograph of arteriole wall, revealing at the top several portions of endothelial cells connected by junctions, basement membrane, smooth muscle cell belonging to tunica media, and various neuronal processes in tunica adventitia. Neuronal vesicles of varying size, shape, and electron density can be seen within these processes. Review the differences between innervation of smooth muscle, cardiac muscle, and skeletal muscle.

D6-D8 Shown in the upper right-hand corner of D6 is a macrophotograph of a small arteriole that has been stimulated with catecholamines. In the region defined by A the smooth muscle is relaxed, whereas at B catecholamines have been topically applied to the surface of the arteriole, which shows marked signs of contraction. Cross-sectional profiles of the vessels as seen by electron microscopy are shown at the left (Region A) and at the right (Region B) of this frame. Higher magnification of the relaxed portion of the arteriole can be seen in D7 and of the contracted portion of the arteriole in D8. In Frame D7 note the flattened, or relaxed, appearance of endothelial cell, the internal elastic lamina, and smooth muscle cells in the tunica media. In Frame D8, observe the scalloped appearance of the endothelial cells, the internal elastic lamina, and the contracted appearance of smooth muscle cells in the tunica media. N, nucleus; E, endoplasmic reticulum; G, granules; IEL, internal elastic lamina; NF, nerve fibers; FIB, fibroblasts; M, muscle; ADV, adventitia; C, collagen; DB, dense bodies; OZ, organelle zone; FEN, fenestration.

D9 Blank

E1 Diagram of microcirculatory unit, arterial portal system, venous portal system, and three types of capillaries found within the body. Fenestrated capillaries are located in tissues where rapid exchange takes place, such as kidney, endocrine glands, and intestine. Sinusoids facilitate exchange of macromolecules and cells; examples are found in liver and hemopoietic organs. Continuous capillaries are found in brain and in muscle. In the microcirculatory unit notice that smooth muscle sphincters are used to control the flow of blood through these vessels.

E2 High-magnification LM of longitudinally sectioned cardiac muscle. Longitudinal profiles of capillaries containing red blood cells can be easily seen. The nuclei of endothelial cells are arranged with their long axis parallel to the flow of blood. (Massons trichrome stain)

E3 Cross-sectional profile of the same field seen in E2. Observe the distribution of capillaries around the muscle fibers and the appearance of the capillaries in cross section. (Massons trichrome stain)

E4 High-magnification LM of capillary in muscle. Notice the orientation of the nuclei and the thickness of the endothelial cells. Red blood cells can be seen en face view as well as in cross-sectional profile. (H & E)

E5 TEM of continuous capillary in smooth muscle. Note the thickness of the endothelial cell wall and the presence of junctions between portions of various endothelial cells.

E6 TEM cross section of fenestrated capillary. Numerous fenestrae can be seen in the endothelial cell wall. Compare this morphology with that of the continuous capillary in E5.

E7 TEM of sinusoidal capillary in liver. Note the gaps within the endothelial cell wall and the lack of a continuous basement membrane around the endothelial cell. The arrow points to a small chylomicron within the lumen of the capillary.

E8 Scanning electron micrograph (SEM) of fenestrated capillary (left) and sinusoidal capillary (right). Observe that fenestrae are present within both types of vessels and that the sinusoidal capillary has large discontinuities within the wall through which can be seen microvilluslike processes of a hepatocyte in the background.

E9 Diagram of large pores and small pores within continuous capillaries and fenestrated capillaries.

F1 Diagram of driving forces and mechanisms involved in pathways taken by plasma molecules diffusing across capillary endothelium. Left side shows fenestrated endothelium; right side, continuous endothelium.

F2 Whole mount of mesentery stained with toluidine blue to reveal presence of mast cells. Note their perivascular distribution.

F3 SEM of surface of three muscle cells. A branching capillary can be seen crossing the field from left to right. Adhering to the surface of the capillaries are extensive cytoplasmic branches of pericytes. C, capillary; P, pericytes; M, muscle cell.

F4 Higher-magification SEM of individual muscle capillary, revealing intimate contact between (1) cytoplasmic processes arising from the body and from the main branch of the pericyte and (2) the surface of the capillary. C, capillary; P, pericytes.

F5 TEM of capillary within muscle, showing relationships of pericyte to capillary wall and to basal lamina. CL, capillary lumen; S, process of the pericyte; P, pericyte.

F6 High-magnification TEM of capillary illustrating junctional contacts between endothelial cell and two smooth muscle cells. These junctions are thought to represent gap junctions which may be involved in metabolic coupling of these cell types. Bm, basement membrane; Mi, mitochondria; Lys, lysosome; Eryth, erythrocyte.

F7 & F8 Frames 7 and 8 illustrate the same small venule in rat mesentery by LM. The fluorescent dye, lucifer yellow, was injected by micropipette into one of the pericytes surrounding this vessel. The dye has spread, presumably via gap junctions, to adjacent coupled pericytes as seen in F8.

F9 LM of small venule showing examples of marginated leukocytes and one neutrophil in the process of diapedesis. (H & E)

G1 LM of postcapillary venule in lymph node. Compare the shape of the endothelial cells in the postcapillary venule with that of capillaries within the same field. (H & E)

G2 TEM of postcapillary venule in lymph node. Note the presence of lymphocytes within the endothelial cell wall, and at the bottom of the field, a single lymphocyte in the process of diapedesis.

G3 LM of small neurovascular unit with peripheral nerve (left), small arteriole (center), and small venule (right). Note the thickness of the walls of the venule and its irregular shape. See A1. (H & E)

G4 TEM of small venule. Observe the relative thickness of the tunica intima, tunica media, and tunica adventitia.

G5 LM illustrating small muscular artery, lymphatic capillary, and small vein. See A1. (H & E)

G6 Higher-magnification LM of cluster of vessels seen in G5. Compare the thickness of wall of the arteriole, lymphatic, and small vein. (H & E)

G7 LM of wall of medium-sized vein. Note relative thickness of tunica intima, tunica media, and tunica adventitia. (H & E)

G8 Low-magnification LM of wall of vena cava. There is circularly arranged smooth muscle in tunica media and longitudinally arranged smooth muscle in tunica adventitia. See A1. (H & E)

G9 Low-magnification LM of wall of vena cava as seen with Verhoeff stain. Observe the distribution of elastin within the wall of the vessel and compare this with that seen in the wall of the aorta in Frame C2 and the muscular artery in D1. The longitudinally arranged smooth muscle in the tunica adventitia is also easily discerned.

Acknowledgments

A8, B4, D2, E9, F1, G4 Reproduced with permission from Nicolae Simonescu and Maia Simonescu, *Histology*, 4th edition, L. Weiss and R. O. Greep, editors, McGraw-Hill, New York, NY, 1977.

B1 Reproduced with permission from Jona C. Thaemert, American Journal of Anatomy 136:62, 1973.

B7, E4 Reproduced with permission from Lennart Nilsson, *Behold Man*, Little, Brown, Boston, MA, 1973.

D4 Reproduced with permission from Melvyn Weinstock, *Histology*, 8th edition, A. W. Ham and D. W. Cormack, editors, Lippincott, Philadelphia, PA, 1979.

D5 Courtesy of Dr. Richard Wood, Department of Anatomy, University of Southern California, School of Medicine, Los Angeles, CA.

D6, D7, D8 Courtesy of Dr. Patricia Phelps, Department of Pathology, University of Maryland, Baltimore, MD.

E6 Courtesy of Dr. David G. Chase, Cell Biology Research Laboratory, Veteran's Administration Hospital, Sepulveda, CA.

E8 Reproduced with permission from P. M. Motta, *The Liver. An Atlas of SEM*, P. M. Motta, M. Muto, T. Fujita, editors, Igaku-Shoin, Tokyo, Japan, 1978.

F3, F4, F5 Courtesy of Drs. Rosemary Mazanet and Clara Franzini-Armstrong, Department of Biology, Faculty of Arts and Sciences, University of Pennsylvania, Philadelphia, PA.

F6 Reproduced with permission from J. A. G. Rhodin, Journal of Ultrastructural Research 18:205, 1967.

F7, F8 Courtesy of Dr. Judson Sheridan, Department of Anatomy, Medical School, University of Minnesota, Minneapolis, MN.

G2 Reproduced with permission from G. D. Levine, *Histology*, 4th edition, L. Weiss and R. O. Greep, editors, McGraw-Hill, New York, NY, 1977.

A1 Diagram illustrating types of lymphatic tissue and lymphatic organs.

A2 Table comparing anatomical locations of T and B lymphocytes in various lymphatic organs and blood.

A3 Diagram depicting route of lymphocyte recirculation between various lymphatic organs.

A4 LM of stratified squamous nonkeratinizing epithelium in vagina. A diffuse infiltration of lymphocytes is seen in the epithelium. (H & E)

A5 LM of intestinal glands showing dense infiltration of lymphocytes in focal region within connective tissue. (H & E)

A6 LM of esophageal epithelium showing entrance of a duct. A small lymphatic nodule can be seen adjacent to the duct and is classified as dense lymphatic tissue. (H & E)

A7 Low-magnification LM of palatine tonsils. Numerous primary and secondary nodules can be seen underlying the epithelium. (H & E)

A8 Higher-magnification LM of palatine tonsil. It shows the stratified squamous nonkeratinizing epithelium, diffuse and dense lymphatic tissue in the connective tissue, and the presence of secondary lymphatic nodules. (H & E)

A9 Still higher magnification of tonsilar epithelium (LM). The diffuse infiltration of lymphocytes into the epithelium obscures the boundary between epithelium and connective tissue. (H & E)

B1 Diagram of lymph node. It includes the capsule, stroma, and parenchyma. Lymph enters the organ through afferent lymphatics, percolates through the cortex and into the medulla by way of sinuses—spaces without an endothelial lining. The lymph exits the organ through efferent lymphatics. Lymph nodes are a site for formation of activated B lymphocytes and serve as a filtration system for lymph.

B2 Low-magnification LM of lymph node showing cortex, medulla, and medullary cords within the latter. Secondary and primary lymphatic nodules can be seen in the cortex just beneath the capsule. (H & E)

B3 Higher-magnification LM of cortex and medulla in lymph node. Secondary nodules can be seen immediately beneath the capsule. Between the secondary nodules and the medulla lies the paracorte. (H & E)

B4 LM illustrating distribution of T and B lymphocytes within secondary nodule in lymph node. In A (left), the tissue has been stained for T cells and the lymphatic nodule is unstained; the tertiary cortex, or paracortex, is heavily stained, indicating that it is a site of concentration of T lymphocytes. In B (right), in which the tissue has been stained for B lymphocytes, the cells of the lymphatic nodule are deeply stained, indicating this is a site of B lymphocyte concentration, whereas only sparse staining for B cells occurs in the paracortex. The staining of the postcapillary venule at the top of this frame demonstrates that B cells move from the postcapillary venule toward the lymphatic nodule.

B5 Autoradiography conducted at LM level (left) or ultrastructural level (right) demonstrates that iodinated antigen (human serum albumin) may persist in dendritic reticular cells for long periods. Antigen is retained by these cells in the outer regions of the nodules, and at the ultrastructural level it can be seen in association with the surface of the cell.

B6 High-magnification LM of secondary nodule immediately underlying capsule of lymph node. Note the presence of both subcapsular and radial sinuses. (H & E)

B7 SEM of lymphatic cortical sinus. Portions of a nodule appear at left. The lumen of the sinus is spanned by reticular cells, and macrophages can be seen adhering to their surfaces. A, arteriole; Rt, reticular cells; M, macrophages; L, lymphocytes. Arrow indicates long processes of reticular cells.

B8 Higher-magnification SEM of lymphatic sinus revealing portion of nodule (upper left). Flattened reticular cells span the sinus lumen, and macrophages with abundant microvillar-like processes adhere to the surfaces of these cells. Rt, reticular cell; M, macrophage.

B9 Blank

C1 LM of postcapillary venules in lymph node. Compare the thickness of the endothelial cell wall with that of capillaries within the field, and observe the presence of lymphocytes within the endothelial wall. (H & E)

C2 TEM of postcapillary venule in thymus. Notice the endothelial cell wall and the presence of lymphocytes within the endothelium. E, endothelial cell; Ly, lymphocytes; Per, pericytes; Ep, epithelial cell. Arrows indicate peripheral margin of the postcapillary venule.

C3 Diagram illustrating lymphatic drainage within the body and entrance of thoracic duct into left subclavian vein.

C4 LM of lymphatic capillary in longitudinal section showing presence of lymphatic valve. (H & E)

C5 LM of lymphatic capillary and adjacent arterioles. Compare the thickness of the wall of the lymphatic capillary with that of the arterioles. (H & E)

C6 TEM of lymphatic capillary. The basement membrane is discontinuous, and the endothelial cell wall is incomplete.

C7 High-magnification TEM showing gaps between adjacent lymphatic endothelial cells. Lumen of lymphatic capillary is at top.

C8 Diagram illustrating structure of thymus.

C9 Low-magnification LM of thymus. It shows the lobular nature of the gland, the presence of a continuous medulla and an incomplete cortex. No nodules are found within the cortex of the thymus. Even at this magnification, Hassall's corpuscles can be seen within the medulla. (H & E)

D1 Higher-magnification LM of cortex and medulla in thymus. A thin capsule can be seen on the surface. The cortex consists of dense masses of lymphocytes, whereas Hassall's corpuscles can be seen within the medulla. (H & E)

D2 TEM of thymic cortex. It reveals large numbers of lymphocytes and the presence of thymic epithelial cells with large vesicular nuclei.

D3 High-magnification LM of thymic medulla illustrating epithelial nature of Hassall's corpuscles. (H & E)

D4 TEM of Hassall's corpuscle in thymus. Prominent tonofilaments are easily seen within the corpuscle. Arrow points to a degenerate lymphocyte. The center of the corpuscle is cystic, and the lining epithelial cells have microvilli. However, none of the epithelial cells within the corpuscle display any secretory apparatus.

D5 Diagram illustrating components of blood-thymus barrier.

D6 TEM of capillary in thymic medulla surrounded by lymphocytes. The basal lamina of the endothelial cell is designated by short arrows; the epithelial cell basal lamina, by long arrows. No endothelial fenestrations are present.

D7 TEM of capillary within thymic cortex five minutes after intravenous injection of horseradish peroxidase. Intense staining for peroxidase is seen within the lumen of the capillary. The endothelial basal lamina, the adventitia, and the intercellular spaces of the surrounding cortical parenchyma are free of peroxidase staining. Nonspecific staining of phagocytic vacuoles within macrophages in the adventitia and within residual bodies is also visible. The inset (upper left) shows part of a capillary within the thymic cortex one minute after the intravenous injection of cytochrome C. The reaction product is seemingly arrested at the intersection between two endothelial cells where junctions are observed. The staining of the red blood cell in the lumen is due to the pseudoperoxidase activity of hemoglobin. RB, residual body. Arrowheads indicate phagocytic vacuoles; single arrow, intercellular junctions between endothelial cells.

D8 TEM of arteriole wall at corticol-medullary boundary in thymus five minutes after intravenous injection of horseradish peroxidase. Reaction product is seen in the clefts of the endothelium, within fenestrations of the elastic interna, and in the adventitia. The inset (upper left) illustrates that the cleft between adjacent endothelial cells stains throughout its length with the same intensity as the blood plasma, indicating this is one of the routes for the diffusion of peroxidase from the lumen into the surrounding adventitial space. A similar staining pattern is also observed within postcapillary venules of the medulla.

D9 Blank

E1 Diagram of splenic circulation.

E2 LM of surface of spleen, illustrating capsule and trabeculae. Examples of red and white pulp are also seen. (H & E)

E3 High-magnification LM of splenic parenchyma, showing course of central artery of white pulp. The periarteriolar lymphatic sheath is visible along this vessel up to where it merges with lymphocytes in the secondary nodule. (H & E)

E4 LM of secondary splenic nodule. Note the eccentric position of the central artery of white pulp. (H & E)

E5 High-magnification LM of red pulp within spleen. A splenic sinusoid is at center. (H & E)

E6 SEM of red pulp of spleen. Examples of three sinusoids are visible. The red pulp between the sinusoids constitutes the cords of Bilroth. The red pulp is supported by reticular cells with extensive processes; lying within their meshwork are macrophages and leukocytes.

E7 SEM of splenic sinusoid. The wall of the sinusoid is composed of rodlike endothelial cells, seen here in cross-fracture. Within the lumen of the sinusoid can be seen a large macrophage and adhering lymphocyte.

E8 SEM of internal surface of splenic sinusoid, illustrating passage of erythrocytes through large gaps in sinusoidal wall. Red blood cells must be flexible in order to constrict their bodies and pass through these fenestrations. Increased rigidity of red blood cells inhibits this passage, and cells thus arrested may presumably be detected by macrophages and thereby removed from the circulation.

E9 TEM of splenic sinusoid and surrounding red pulp. Red blood cells and various types of leukocytes can be seen within the red pulp, and one cell appears to be in the process of diapedesis. S, sinusoid; R, red blood cell; E, endothelial cell; L, lymphocytes; M, macrophage; P, polymorph; PL, plasma cell. Double arrows indicate process of reticular cell. Single arrow points to cell migrating through perforation in the sinusoidal wall.

F1 TEM of white pulp in spleen. Dendritic cells are a distinct subpopulation of spleen cells whose identification is based on cytological features in the absence of critical lymphocyte and macrophage traits. These cells lack surface immunoglobulin as well as thymic and brain antigens and do not respond to lipopolysaccharide or concanavalin A in vitro. Dendritic cells are important because they stimulate the mixed leukocyte reaction and interact with T cells. Dendritic cells have irregularly shaped nuclei, and the cytoplasm contains few organelles and an electron lucent matrix. Dendritic cells are also frequently related to connective tissue cell processes and/or reticular fiber deposits. De, dendritic cell; SL, small lymphocytes; En endothelial cell; *, processes of dendritic cells.

F2 TEM of dendritic cell and macrophage in white pulp of spleen. Dendritic cells are found only in the white pulp and can be distinguished from macrophages by the ability of the latter to interiorize large amounts of colloidal thorium dioxide, as shown in this micrograph. Colloidal thorium is present in the intercellular space between the two cells (arrows); however, only the macrophage has internalized large amounts of this tracer. Compare with dendritic cell seen in Frame B5. De, dendritic cell; Mac, macrophage; Ly, lysosome; RER, rough endoplasmic reticulum.

F3 Diagram illustrating mononuclear phagocyte system and its function in a variety of tissues.

F4-F9 Blank

G1 Diagram of cytological features of thick skin (left) and thin skin (right). Hair follicles are associated with thin skin. Note that the inner root sheath is not seen above the level of the sebaceous gland. Capillaries do not invade the epidermis; nutrients cross into the epidermis by diffusion. Naked nerve endings (pain), however, are seen in the epidermis.

G2 Low-magnification LM of thick skin. Observe the thickness of each of the layers: stratum germinativum, stratum spinosum, stratum granulosum, and stratum corneum. (H & E)

G3 Higher-magnification LM of epidermis in thick skin. Cells in the stratum germinativum rest on the basement membrane, and their long axis is perpendicular to it. As cells migrate into the stratum spinosum, this orientation is lost. Basophilic keratohyaline granules can be seen demarcating the stratum granulosum. (H & E)

G4 LM of thin skin. Compare the thickness of each layer with that seen in thick skin in G2. (H & E)

G5 LM of thin skin treated with dilute sodium hydroxide to swell the stratum corneum. Observe that cells in the stratum corneum are arranged in rows or columns and that there appears to be a preferred migration route from the stratum germinativum to the surface of the stratum corneum. (toluidine blue stain)

G6 SEM of epidermis and papillary dermis. Note the boundary between papillary dermis and underlying reticular dermis, the latter containing coarser collagen bundles. The different layers of the epidermis can be identified, and a small vessel can be seen immediately beneath the epidermis.

G7 TEM of full thickness of epidermis. Basal, spinous, granular, and cornified layers are evident. There is only a single granular layer, and in this section none of these cells show a nucleus. Note the greater number of desmosomes within the stratum spinosum.

G8 TEM of stratum germinativum in skin. Note the presence of desmosomes on the lateral and apical boundaries. A portion of the papillary dermis can be seen (lower left).

G9 High-magnification TEM of stratum germinativum showing hemidesmosomes that anchor these cells to basement membrane. In the papillary dermis, small anchoring fibrils attach themselves to the basal lamina. At the sites of hemidesmosome attachment to the basal lamina, small threadlike strands course from the hemidesmosome into the basal lamina. A small unmyelinated nerve fiber is located close to the epidermis.

Acknowledgments

A3, F3 Reproduced with permission from J. H. L. Playfair, *Immunology at a Glance*, 2d edition, J. H. L. Playfair, editor, Blackwell Scientific Publications, Osney Mead, Oxford, England, 1982.

B4 Reproduced with permission from Irving L. Weissman, Transplantation Review 24:159, 1975.

B5 Courtesy of Dr. T. E. Mandel, Hall Institute of Medical Research, University of Melbourne, Victoria, Australia.

B7, B8, E8 Reproduced with permission from Tsuneo Fujita, *SEM Atlas of Cells and Tissues*, T. Fujita, K. Tanaka, and J. Tokunaga, editors, Igaku-Shoin, Tokyo, Japan, 1981.

C2 Reproduced with permission from Wei S. Hwang, Laboratory Investigation 31:481, 1974.

C6, C7 Courtesy of Dr. Lee Leek, Department of Anatomy, Howard University College of Medicine, Washington, DC.

D2 Reproduced with permission from Tatsuo Ebe and S. Kobayashi, Fine Structure of Human Cells and Tissues, T. Ebe and S. Kobayashi, editors, Igaku-Shoin, Tokyo, Japan, 1972.

D4 Reproduced with permission from R. M. Bearman, Anatomical Record 190:769, 1978.

D6 Reproduced with permission from R. M. Bearman, Anatomical Record 183:495, 1975.

D7, D8 Reproduced with permission from Elio Raviola, Journal of Experimental Medicine 136:466, 1972.

E6, E7 Reproduced with permission from Tsuneo Fujita, Archivum Histologicum Japonicum 37(3):187-216, 1974.

E9 Reproduced with permission from Ramon Pictet, Zeitschrift Zellforschung 96:383, 1969.

F1, F2 Courtesy of Dr. Ralph M. Steinman, Department of Immunology, The Rockefeller University, New York, NY.

F8 Courtesy of Drs. Gary Gorbsky, Hisato Shida, and Malcolm Steinberg, Department of Biology, Princeton University, Princeton, NJ.

G5 Courtesy of Dr. Ian Mackensie, School of Dentistry, University of Iowa, Iowa City, IA.

G6, G7, G9 Courtesy of Dr. Karen Holbrook, Department of Biological Structure, University of Washington School of Medicine, Seattle, WA.

G8 Courtesy of Dr. Paul C. Letourneau, Department of Anatomy, Medical School, University of Minnesota, Minneapolis, MN.

A1 High-magnification LM of thick skin showing stratum germinativum, stratum spinosum, and stratum granulosum. (H & E)

A2 Indirect immunofluorescent staining of frozen sections of stratified squamous epithelium, using mouse antiserum prepared against bovine desmosomal glycoproteins. Observe that epithelial cell borders are stained in a highly punctate pattern characteristic of the distribution of desmosomes.

A3 TEM depicting stratum spinosum, stratum granulosum, and stratum corneum. Numerous desmosomes are at the margins of cells in the stratum spinosum. Electron-dense deposits representing keratohyaline granules are seen in the stratum granulosum. In the stratum corneum, no recognizable cell organelles are detected owing to cellular degradation. The cells are still interlocked at all margins, even though junctions are modified and fewer in number as compared with the stratum spinosum.

A4 High-magnification TEM of desmosome tonofilament complexes in spinous layer of epidermis. Tonofilaments predominantly in transverse section course through the cytoplasm toward the dense desmosomal plaques. M, midline; T, tonofilaments.

A5 LM illustrating stratum spinosum, stratum granulosum, and stratum corneum. Observe the lack of nuclei and other recognizable cytological features in the stratum corneum. (H & E)

A6 Low-magnification TEM of spinosum, granular, and lower cornified cells of epidermis (left). The left micrograph shows the keratohyaline granules to good advantage and reveals that the electron-dense material is deposited in the interstices of the keratin filaments. Lamellar granules can be seen in all the viable epidermal cells. High-magnification TEM of portions of granular and cornified cells (right). Easily seen at high magnification (right) are the association of keratohyaline granules with keratin filaments, the cornified cell envelope, the absence of organelles from the cornified cell, and its association with other cornified cells by modified desmosomes. Lamellar granules are present in the cytoplasm of the granular cell and discharge their contents into the extracellular space by the process of exocytosis. An example of this is seen at the left-hand margin of the picture.

A7 Diagram of melanocyte and formation of melanin. The melanocyte is located beneath or between the cells of the basal layer of the epidermis. These cells are of neural-crest derivation and synthesize the skin pigment melanin which absorbs UV light damaging to DNA. In melanosomes, the enzyme tyrosinase, a copper-containing aerobic oxidase, is the enzyme responsible for the conversion of both the naturally occurring amino acid tyrosine to dihydroxyphenalalanine (DOPA) and DOPA to DOPA quinone. Melanin synthesis is completed within the melanosomes, and the melanin granules are then transported through the dendritic processes, secreted, and taken up by adjacent keratinocytes.

A8 Whole mount of frog skin incubated for DOPA reaction. Melanocytes appear as a discontinuous network of dendritic cells whose processes fan out in all directions.

A9 TEM of melanocyte resting on basal lamina and flanked by keratinocytes. Note that the melanocyte does not form hemidesmosomes with the basal lamina or desmosomes with the keratinocytes. There are few melanosomes in the cytoplasm. This is characteristic; most melanosomes are transferred to the keratinocyte. The melanocyte does not have keratin filaments but does contain another class of intermediate filaments, which are evident in this micrograph.

B1 TEM of melanocyte from a black individual, showing melanosomes in both melanocyte and adjacent keratinocytes. Again the absence of specific junctions between melanocytes and keratinocytes and the basal lamina are evident. This also correlates with what is seen histologically; the melanocytes are pale cells as compared with surrounding keratinocytes.

B2 High-magnification TEM of melanosomes in melanocyte from hair follicle. The matrix structure upon which pigment is synthesized is apparent.

B3 LM of thin skin from a black individual. Note the presence of melanin in the basal cells. (H & E)

B4 TEM of full-thickness epidermis from a black individual. Note the amount of pigmentation in the basal keratinocytes and the small amount of melanin in the suprabasal cells. There is degradation of pigment in the melanosome complexes as differentiation progresses, although some pigment is always retained. In this micrograph melanin can be seen even in some of the cornified cells.

B5 Diagram illustrating four biological processes underlying melanin pigmentation. These are melanosome formation, melanosome melanization, melanosome secretion, and melanin degradation. In the Caucasian epidermal cell, or keratinocyte, groups of melanosomes are aggregated within membrane-limited, lysosomelike organelles, and the melanosomes often appear fragmented. However, in the Negroid epidermal cell, the melanosomes remain discrete. Skin pigmentation is a function of (1) tyrosine activity in the melanosomes, (2) the degree of melanosome pigmentation, and (3) the degradation of the melanosomes as they migrate in keratinocytes toward the surface. The number of melanocytes found in the skin of Caucasians, Negroids, and Mongoloids is relatively constant, averaging approximately 2,000 melanocytes/square mm on the head and forearm and 1,000 melanocytes/square mm on the rest of the body.

B6 TEM of stratum spinosum. Several keratinocytes and two Langerhans cells can be seen. The Langerhans cells are recognized by the convoluted nuclear contour and by the characteristic granules in the cytoplasm (seen best in the denser of the two cells). The keratinocytes show abundant keratin filaments in the cytoplasm (only microfilaments are present in the Langerhans cells) and desmosomes. The Langerhans cells do not form attachments with adjacent keratinocytes.

B7 High-magnification TEM of Langerhans cell showing structure of Langerhans cell granule. There is also a large membrane bound structure which appears to contain microtubules or some tubular structure. Langerhans cells often contain material in phagocytic vacuoles.

B8 TEM of basal region of epidermis showing Merkel cells. A characteristic feature of the Merkel cell is the presence of round, electron-dense granules located mainly on the opposite side of the nucleus to the Golgi apparatus. The Merkel cell, unlike the melanocyte and the Langerhans cell, is connected to surrounding keratinocytes by desmosomes. Merkel cells are usually closely associated with germinal neurites and are thought to form a complex that serves as a touch receptor. Figure 3 is a high magnification of the Merkel cells seen in Figure 2.

B9 Blank

C1 Low-magnification LM of hairy skin. Examples of sebaceous glands, sweat glands, and arrector pili muscle, as well as shafts of hair, can be seen. (H & E)

C2 LM of hair follicles from scalp. In the longitudinally sectioned hair, identify the papilla, connective tissue sheath, inner root sheath, outer root sheath, and shaft of the hair. (H & E)

C3 LM of lower, bulb-shaped portion of hair. Identify the matrix that is the germative center of the hair. The papilla and the connective tissue sheath are also visible. (H & E)

C4 LM illustrating above the matrix the emerging hair and the concentric outer and inner root sheaths. (H & E)

C5 LM showing longitudinal section of hair above entrance of sebaceous gland. The hair itself is composed of a cuticle, cortex, and medulla. The entire follicle is encased by a connective tissue sheath. Identify the outer root sheath. (H & E)

C6 LM of upper portion of hair follicle where it emerges onto surface of skin. The outer root sheath is continuous with the epidermis, and squames of keratin extend into the well of the hair shaft. (H & E)

C7 SEM of hairy skin.

C8 SEM showing emergence of hair shaft from stratified squamous keratinizing epithelium. Compare with C6.

C9 LM showing longitudinal section of hair shaft and opening of sebaceous gland into hair shaft. Observe the arrector pili muscle. (H & E)

D1 High-magnification LM of sebaceous gland. Outermost cells of the gland rest on a basal lamina comparable to that of the epidermis. These basal cells are the germinative cells of the gland. As the cells migrate toward the center of the gland, they progressively accumulate lipid within their cytoplasm. The cells continue to enlarge, their nuclei become distorted and disintegrate, and eventually the cells lyse, thus forming sebum, the lipid product of the glands. (H & E)

D2 TEM of edge of sebaceous gland. Note the less differentiated germinative cells at periphery of the gland. Lipogenesis is evident in cells removed from the periphery of the gland.

D3 LM of sweat gland showing coiled sweat ducts and secretory portions of the gland. The secretory portions exhibit a larger diameter, whereas the ducts are smaller and stained more intensely. (H & E)

D4 TEM of eccrine sweat gland. The secretory tubule in the sweat gland is composed of three distinct cell types: myoepithelial cells, clear serous cells, and dark serous cells. The dark cells contain secretory granules that vary in electron density and which are believed to be made up of mucosubstance. The clear cells (lower left) contain abundant glycogen particles and are thought to produce most of the watery secretion that emerges as sweat on the surface of the skin. The lumen of the secretory tubule can also be seen (upper left).

D5 LM of dermis through which duct of sweat gland passes as it courses to surface of skin. The dermis can be subdivided into the papillary layer adjacent to the epidermis and the thicker, reticular layer which extends to the underlying fatty hypodermis. (H & E)

D6 TEM of duct of sweat gland. The duct of a sweat gland consists of two layers of cells: the basal, or peripheral, cells which contain numerous mitochondria and the superficial cells which lie closest to the lumen and form the cuticular border (arrows). The duct does not contain myoepithelial cells nor are there secretory cells of either serous or mucous types. Physiological studies show that the duct of the eccrine sweat gland is engaged in the active resorption of sodium, which is excreted by the secretory tubules. BM, basement membrane; P, peripheral cells; S, superficial cells; Lu, lumen of the duct.

D7 TEM of basal surface of epidermis. Neurite processes enveloped by Schwann cells can be seen fusing with the basal surface of the epidermis. The basal lamina of the epidermis is continuous with that surrounding the Schwann cells. a, neurite process; K, keratinocyte; BL, basal lamina; Sc, Schwann cell.

D8 LM of thick skin with Meissner's corpuscle in dermal papilla of connective tissue. (H & E)

D9 LM of hypodermis showing Pacinian corpuscle. (H & E)

E1 Diagram of development of exocrine and endocrine glands. The invagination of epithelial cells results in the formation of glands. If a connection with the surface persists (in the form of a duct), the organ is an exocrine gland (B). If the connection disappears, the gland is endocrine and discharges its secretory product into the blood vascular system (C). Unicellular glands may be found in simple epithelium (A), such as the intestinal epithelium.

E2 LM of intestinal epitheium. The goblet cell is an example of a unicellular gland that secretes a sulfated mucin. (H & E)

E3 LM of base of intestinal crypt in intestine. The clustering of Paneth cells in the base of the gland is an example of a simple multicellular gland. (H & E)

E4 LM of surface epithelium in stomach. The entire epithelial surface consists of surface mucous cells, each of which elaborates its product into the lumen of the stomach. In this instance the entire surface epithelium functions as a multicellular gland. (H & E)

E5 Diagram illustrating the structure and activities of exocrine glands and the duct systems used to drain them. Ducts are described as intralobular when they lie within the lobule, whereas interlobular ducts lie in the connective tissue between lobules and drain secretions from several adjacent lobules. Salivary glands may have serous secretions such as in the parotid, or mixed seromucous secretions as in the submandibular and sublingual glands. The pancreas is a serous-secreting gland.

E6 Low-magnification LM of parotid gland showing both serous acini and large amounts of fat infiltration. Intralobular ducts can be seen in center of lobule. (H & E)

E7 LM of parotid lobule, with intercalated duct (upper left) and striated duct (lower right). The nuclei of the basophilic serous cells can be seen at the periphery of the acini. (H & E)

E8 TEM of parotid acini from unstimulated gland, showing serous cells with numerous secretory granules surrounding central lumen (upper right). Compare with E9.

E9 TEM of parotid gland acini after sympathetic stimulation. Note the extensive depletion of acinar secretion granules and the prominence of the basal rough endoplasmic reticulum.

F1 Diagram of neural regulation of exocrine secretion. The autonomic nervous system innervates exocrine glands by means of its sympathetic and parasympathetic divisions. Neurons of the sympathetic nervous system tend to travel in company with blood vessels, whereas those of the parasympathetic nervous system follow the ducts.

F2 TEMs of innervation of parotid acinar cell. Panel A shows an unmyelinated nerve terminal beneath the basal lamina. In panel B an unmyelinated nerve terminal has also penetrated the basal lamina and lies within an inpocketing of the acinar cell. Arrows indicate subsurface cisternae. LV, large vesicle.

F3 TEM of parotid acinar cell. Secretion granules are polarized toward the lumen of the secretory channel. In the base of the cell are multiple arrays of rough endoplasmic reticulum and several lysosomes. The lateral cell membranes are interdigitated, while the basal surface of the cell rests on the basement membrane. L, lumen; LY, lysosome; G, Golgi; CV, condensing vacuole; SG, secretion granule; N, nucleus.

F4 TEM of interface between exocrine cells in acinus and intercalated duct cells. EExS, exocrine lumen extracellular space; DC, duct cell.

F5 TEM of exocrine acinus-intercalated duct junction. Observe the connection of the intercalated duct cells to the acinus. Compare this with the LM of intercalated ducts seen in F6.

F6 LM of parotid lobule showing intercalated and striated ducts intermixed between serous acini. Several fat cells, or adipocytes, are also present. (H & E)

F7 LM of striated duct. Cells lining the duct are columnar, with a centrally located nucleus. (H & E)

F8 TEM of striated duct in parotid gland. Note the abundant numbers of mitochondria within the basal cytoplasm of the cell.

F9 LM of interlobular ducts. Large amounts of collagen invest the interlobular ducts as they course between adjacent lobules of glandular tissue. (H & E)

G1 LM of extralobular duct with stratified epithelium surrounded by substantial connective tissue. (H & E)

G2 LM of seromucous gland illustrating serous demilunes. (H & E)

G3 TEM of serous demilune. Mucous cells contain electron-lucent granules, whereas the serous cells located at the periphery of the mucous units contain electron-dense granules and substantial amounts of rough endoplasmic reticulum. Large arrows indicate processes of myoepithelial cells.

G4 Indirect immunofluorescent localization of myosin in myoepithelial cells surrounding serous acini. Note the radial, or dendritic, appearance of myoepithelial cells (right of center) in these tangentially sectioned acini. Compare with G8.

G5 Low-magnification LM of submandibular gland showing interlobular ducts and secretory lobules. (H & E)

G6 Higher-magnification LM illustrating serous and mucous secretory units in submandibular gland. A portion of a striated duct can be seen (left). Note the presence of serous demilunes. (H & E)

G7 Low-magnification LM of sublingual gland illustrating interlobular ducts and presence of intralobular ducts within glandular lobule. (H & E)

G8 High-magnification LM of sublingual gland showing mucous acini surrounded by myoepithelial cells. A few serous cells are also present in some acini. (H & E)

G9 TEM of sublingual gland acini showing both mucous cells and serous-secreting cells. A myoepithelial cell is visible at periphery of acinus.

Acknowledgments

A2 Courtesy of Drs. Gary Gorbsky, Hisato Shida, and Malcolm Steinberg, Department of Biology, Princeton University, Princeton, NJ.

A4 Courtesy of Drs. Christine Skerrow and David Skerrow, Department of Dermatology, University of Glasgow, Glasgow, Scotland.

A3, A6, A9, B1, B2, B4, B6, B7, D2 Courtesy of Dr. Karen Holbrook, Department of Biological Structure, University of Washington School of Medicine, Seattle, WA.

A8 Courtesy of Dr. Paul C. Letourneau, Department of Anatomy, Medical School, University of Minnesota, Minneapolis, MN.

B5 Reproduced with permission from *Dermatology in General Medicine*, T. B. Fitzpatrick et al., editors, McGraw-Hill, New York, NY, 1971.

B8 Reproduced with permission from P. J. Garant, American Journal of Anatomy 157:155, 1980.

D4, D6 Reproduced with permission from Richard A. Ellis, *Ultrastructure of Normal and Abnormal Skin*, A. S. Zelickson, editor, Lea and Febiger, Philadelphia, PA, 1967.

D7 Reproduced with permission from Lawrence Kruger, Journal of Comparative Neurology 198:144, 1981.

E8, E9 Courtesy of Dr. J. R. Garrett, Department of Oral Pathology and Oral Medicine, Dental School, Kings College Hospital Medical School, London, England.

F2 Reproduced with permission from Arthur R. Hand, Anatomical Record 173:135, 1972.

F3 Reproduced with permission from Arthur R. Hand, American Journal of Anatomy 135:81, 1972.

F4 Reproduced with permission from Robert P. Bolender, Journal of Cell Biology 61:269, 1974.

F5 Courtesy of Dr. I. Joel Leeb, Department of Endodontics, School of Dentistry, University of North Carolina, Chapel Hill, NC.

F8 Reproduced with permission from Bernard Tandler, Anatomical Record 184:115, 1976.

G3, G4 Reproduced with permission from Carlin A. Pinkstaff, International Review of Cytology 63, 1980.

G9 Courtesy of Dr. Robert S. Redman, Dental Service, Veteran's Administration Hospital, Washington, DC.

A1 Low-magnification LM of pancreas. Pale clusters of endocrine cells comprising islets of Langerhans can be seen interspersed among the serous acini. (H & E)

A2 High-magnification LM of pancreas. Serous pancreatic acini surround a well-vascularized islet of Langerhans. Because of their staining properties, intralobular ducts are difficult to find within the pancreatic lobules. (H & E)

A3 Indirect immunofluorescent micrograph showing localization of the pancreatic enzyme amylase. Specific staining for amylase is seen within the secretory granules of the serous acinar cells, which are polarized toward the lumen of the secretory channel.

A4 High-magnification LM illustrating structure of pancreatic acinus. The acinus at the top contains centrally located nuclei which are the beginnings of the intercalated duct. These cells are referred to as centroacinar cells. (H & E)

A5-A9 Blank

B1 Diagram illustrating relationships between hypothalamus and anterior and posterior lobes of pituitary gland. The anterior pituitary is derived from pharyngeal epithelium and consists of three parts: the pars distalis, which comprises the bulk of the gland and produces six hormones; the pars intermedia, which is a very thin portion of the anterior pituitary found posterior to Rathke's cysts in the adult; and the pars tuberalis, an extension of the anterior pituitary which wraps around the neural stalk. The hypothalamic hypophyseal portal system transports releasing factors and inhibiting factors from the hypothalamus via the bloodstream to the pars distalis where they influence the secretion of pituitary hormones. The posterior pituitary (pars nervosa) is an evagination of the hypothalamus and is the site of storage and release of the hormones oxytocin and vasopressin, which are synthesized by cell bodies in the hypothalamus. The hypothalamohypophyseal tract consists of axons, mainly from the paraventricular and supraoptic nuclei, which transport hormones to the pars nervosa for storage (in Herring bodies) and release. Pituicytes are supporting (glial-like) cells of the pars nervosa.

B2 Macrophotograph of pituitary gland. The large pars distalis portion of the pituitary gland consisting of acidophilic and basophilic cells is easily distinguished from the pale-staining pars nervosa. (H & E)

B3 LM of pars distalis illustrating cord like arrangements of cells and sinusoidal vessels. Three cell types can be recognized: the acidophil, the basophil, and the chromophobe. The first two are recognized by their tinctorial staining properties and produce six different hormones, whereas the chromophobe is characterized by a lack of staining. The term chromophobe is widely used in the pathology literature but is now known to represent either an acidophil or basophil with only a few secretory granules. (H & E)

B4 LM of pars distalis stained with Masson's trichome. The distinction between acidophils and basophils is very easily made. Some cells representing the chromophobe are also seen, but these cells are known to represent one of the six hormonal cell types.

B5 LM of section of pituitary immunocytochemically stained for growth hormone. The dark brown-staining oval cells are somatotropes and comprise one of the two acidophil cell types found within the pituitary.

B6 TEM of pars distalis showing somatotropes. These cells are characterized by the presence of large, round, secretory granules.

B7 TEM immunocytochemical localization of growth hormone at ultrastructural level. Specific staining for growth hormone can be seen within the large secretion granules.

B8 LM of section of pituitary stained for the hormone prolactin. The prolactin cell, or mammotrope, is irregular in shape and is also a member of the acidophil class of pituitary cells.

B9 TEM of pars distalis showing mammotrope (or prolactin) cell, which contains large, irregular-shaped granules.

C1 TEM of cell in pars distalis that secretes thyroid stimulating hormone (TSH). This cell type belongs to the basophil group and is characterized by the presence of numerous small granules which are marginated toward the plasmalemma.

C2 TEM of pituitary illustrating immunocytochemical localization of TSH within small secretory granules of TSH cell. The staining for TSH was accomplished on the thin section, and the specific staining is recognizable by the presence of small stain complexes overlying the secretion granules. This is better seen in the inset (lower right).

C3 TEM of adrenocorticotropic hormone (ACTH) cell. The ACTH cell is also a member of the basophil class. This cell is stellate shaped, and one process can be seen extending toward the right side of thr frame. Small granules are near the plasmalemma. In the human, this cell type is also PAS-positive since the prohormone for ACTH is a glycoprotein, whereas the circulating form of ACTH is a polypeptide.

C4 TEM of gonadotrope. The gonadotropin-secreting cells in the pituitary are also basophils. These cells secrete LH and FSH, and some evidence suggests that one cell may secrete both hormones.

C5 LM of pars distalis. This pituitary gland was obtained from a woman who had been both ovaryectomized and adrenalectomized. Since the target organs for both ACTH and the gonadotropin hormones were removed, the basophilic gonadotropes and ACTH cells continue to hypertrophy and have formed what are called either adrenalectomy or castration cells. An example of a large basophil is seen in the center of this frame. (Masson's trichome stain)

C6 TEM of castration cell in pars distalis of rat. Owing to the removal of the target gland by castration, this gonadotropin cell has enlarged, as evidenced by the hypertrophied rough endoplasmic reticulum. The cell is attempting to produce more gonadotropin to stimulate the gonads to secrete steroid hormones. Since the gonads were removed by castration, the production of steroids is impossible, and the cell thereby is unable to shut off production of gonadotropin hormones.

C7 LM showing pars distalis, Rathke's cyst, intermediate lobe, and pars nervosa. That portion of the pars distalis posterior to Rathke's cyst is the intermediate lobe. (Masson's trichrome)

C8 Higher-magnification LM of pars nervosa showing pituicytes, endothelial cells, and Herring bodies. In this Masson's trichome stain, the Herring bodies can be recognized by their blue, smooth, homogenous-staining appearance.

C9 TEM of pars nervosa stained at ultrastructural level for vasopressin. Note immunoreactive deposits over axons and nerve terminals, the latter corresponding to Herring bodies at the LM level. The inset shows, at high magnification, specific staining for vasopressin only over secretory granules within the terminals and axons.

D1 Diagram of TSH-induced synthesis and secretion of thyroxin in thyroid gland. The thyroid gland stores its product in a colloidal pool within the follicle rather than in the cell itself. Secretion of thyroxin involves the uptake of the colloidal product from the lumen of the follicle, its breakdown within lysosomes in the thyroid cells, and its release into the bloodstream.

D2 LM of thyroid gland showing ball-like arrangements of thyroid cells and presence of colloid within central lumen. (H & E)

D3 LM of thyroid stained with PAS technique. Thyroglobulin is a glycoprotein and therefore appears as an intense red with this staining method.

D4 TEM of thyroid follicle. Colloid can be seen in the lumen of the thyroid follicle (left). The thyroid follicular cells are cuboidal and relatively inactive. Several dense bodies are visible in the base of the thyroid follicular cells. A fenestrated capillary can be seen in the connective tissue surrounding the thyroid follicle.

D5 SEM of vascular cast of thyroid gland. Note the tortuous arrangement of capillaries around the follicle. The basketlike arrangement of capillaries is indicative of the high vascularity of the thyroid gland.

D6 LM of group of thyroid follicles. Observe the large central follicle which shows a scalloping of the colloid within the lumen. The scalloping indicates increased secretory activity of the columnar cells lining this follicle, whereas the follicle immediately to the left has a smooth colloid appearance at its periphery and the cells are low cuboidal to squamous and inactive. (H & E)

D7 SEM of luminal surface of thyroid follicle. Note the microvillous surface of the thyroid follicular cells in the resting state (left). The thyroid follicle (right) has been stimulated with the hormone TSH. Observe the exensive pseudopods and veil-like extensions of the apical cytoplasm of these cells into the follicular lumen. The cytoplasmic extensions are involved in the phagocytic uptake of colloid into the thyroid follicular cell.

D8 LM of thyroid gland stained for the hormone thyrocalcitonin. Cells that are stained dark brown contain thyrocalcitonin and are located in the wall of the thyroid follicle.

D9 TEM of thyroid follicle wall showing presence of thyrocalcitonin cell. Observe the small dark secretory granules that are polarized toward the connective tissue surface of the follicular wall (lower left).

E1 Diagram illustrating role of parathyroid gland and other organs in regulation of serum calcium.

E2 LM of parathyroid gland. This gland often shows fatty infiltration. The parenchyma of the gland consists of three cell types: small, dark-staining chief cells; larger, red-staining oxyphil cells; and clear-staining Wasserhelle cells. (H & E)

E3 Higher-magnification LM of parathyroid gland. The frame shows chief cells, oxyphil cells, and clear cells (or Wasserhelle cells). (H & E)

E4 LM illustrating immunocytochemical localization of parathormone in chief cells of parathyroid.

E5 TEM of parathyroid gland showing chief cell. Unlike other endocrine cell types, the chief cell is characterized by the relative absence of secretory granules since it does not contain a large amount of parathormone in storage form.

E6 TEM of oxyphil cells in parathyroid. Note the abundant mitochondria which almost completely fill the cytoplasm of this cell type.

E7 Diagram of architecture and blood flow through adrenal gland, subdivisions of adrenal cortex, and principal hormones secreted in each. Secretion in the adrenal gland is regulated by ACTH from the anterior pituitary gland and by renin from the kidney (for the cortex) and by preganglionic sympathetic neurons (for the medulla). An occasional postganglionic neuron may be found in the adrenal medulla, while the chromaffin cells of the medulla are modified, postganglionic sympathetic neurons of neural-crest derivation. Medullary secretion is modified by glucocorticoids and methyltransferase transported to the medulla by the cortical sinusoids. Medullary arterioles carry fresh blood directly to medullary capillaries. Both sets of vessels are drained by collecting medullary veins into the suprarenal veins which transport adrenal hormones into the peripheral circulation.

E8 Macrophotograph of adrenal gland. Zonation of the adrenal cortex and the presence of the medulla can easily be distinguished. Large collecting veins are also recognizable within the medulla. (H & E)

E9 Low-magnification LM of adrenal gland. At left is the capsule containing a small amount of pericapsular fat. Immediately beneath the capsule is the zona glomerulosa, then the zona fasiculata and the acidophilic-staining zona reticularis. At the right can be seen the basophilic-staining medulla in which several large collecting veins are present. (H & E)

F1 Higher-magnification LM of zona glomerulosa of adrenal gland. The capsule of the gland is seen at left, and continuation of the zona glomerulosa (round clusters of cells) into the zona fasciculata is seen at right. (H & E)

F2 TEM of zona glomerulosa. Cells of the zona glomerulosa contain abundant, smooth endoplasmic reticulum in the cytoplasm, and elongated mitochondria with broad, flattened cristae. Small amounts of lipid and lipofuscin pigment are also present.

F3 LM of adrenal cortex illustrating junction between zona fasciculata (left) and zona reticularis (right). Note the vacuolated cytoplasm in the zona fasciculata, indicating the presence of large amounts of lipid. (H & E)

F4 TEM of zona fasciculata showing long, radially arranged cords of cells and adjacent fenestrated capillaries. D, lipid droplets; S, extravascular space; C, capillary lumen.

F5 TEM of zona fasciculata cells at higher magnification. These cells are characterized by the large number of lipid droplets and distinctive mitochrondria which contain short tubular cristae. The cytoplasm also contains well-developed smooth endoplasmic reticulum and occasional patches of rough endoplasmic reticulum.

F6 TEM of zona fasciculata cells at still higher magnification. The tubular cristae in the mitochondria are easily discerned. Also note the abundant, smooth endoplasmic reticulum and the presence of lipofuscin pigment and small patches of rough endoplasmic reticulum.

F7 LM illustrating junction between zona reticularis and adrenal medulla. Cells in the zona reticularis are compact and more intensely stained than those in the zona fasciculata. These cells also contain sizable amounts of lipofuscin pigment, which is visible as gold-brown deposits located near the nuclei. (H & E)

F8 TEM of junction between zona reticularis and adrenal medulla. Observe the residual bodies present within the zona reticularis cells. The granulated cells of the adrenal medulla are seen at right. D, lipid droplet; Ep, epinephrine-producing cell; N, nucleus; Nor, norepinephrine-producing cell; S, sinusoid; and *, intercellular space.

F9 Higher-magnification TEM of cells in zona reticularis. Note the many residual bodies and sizable number of mitochondria within the cell. Smaller numbers of lipid droplets are present in the zona reticularis cells, and the smooth endoplasmic reticulum is not quite as well developed as in the zona fasciculata.

G1 LM of adrenal medulla showing chromaffin cells and two sympathetic postganglionic cells in center of frame. (H & E)

G2 TEM of adrenal medulla showing different granule types within norepinephrine- and epinephrine-secreting cells. Epinephrine-secreting cells contain granules that exhibit only slight to moderate electron density owing to the fact that epinephrine is extracted from the tissue during fixation and processing. Norepinephrine reacts with glutaraldehyde, a fixative used in TEM, to produce an electron-dense polymer and accounts for the electron density seen in this granule type. NE, norepinephrine; E, epinephrine.

G3 LM of aldehyde fuchsin-stained pancreas demonstrating selective staining for insulin within beta cells of islets of Langerhans. Observe that some cells within the islet are unstained with this procedure.

G4 Immunocytochemical staining for insulin and glucagon of islet of Langerhans in pancreas (LM). The insulin-producing beta cells are stained with a blue reaction product and form cordlike clusters of cells. The brown-staining alpha cells, which contain glucagon, are seen at the periphery of the islet. See G5 for the staining of somatostatin cells and their location within the adjacent section of the same islet.

G5 LM of the same pancreatic islet seen in G4 but stained for glucagon and somatostatin. The alpha cells, which contain glucagon, are stained brown, as they were in G4, and the somatostatin cells are now stained blue. Note that these cells are also found at the periphery of the clusters of beta cells.

G6 High-magnification TEM of an islet of Langerhans in pancreas. Each cell type in the pancreatic islet has a distinct granular morphology. The beta cells (B) contain both a core with moderate electron density and a nonstaining halo. The alpha cells (A) contain an electron-dense core and an eccentric halo. The D-1 cell, or somatostatin-producing cell, contains granules with moderate electron density and no halo. The D cell (now called PP cell), at top of frame, contains the hormone pancreatic polypeptide.

G7 TEM showing thin sections and freeze fracture of beta cells (arrowheads). The thin section at left shows a punctate contact between two beta cells that is thought to correspond to gap junctions (arrowheads) seen by freeze fracture.

G8 LM localization of lucifer yellow (left) in cells showing dye transfer (gap junctions) and localization of insulin (right). Note that not all lucifer yellow-positive cells contain insulin; therefore gap junctions are present between beta and nonbeta cells.

G9 Diagram showing relationship between gap junctions and innervation of pancreatic islet cells.

Acknowledgments

A3, G7 Courtesy of Dr. Paolo Meda, Institute of Histology, University of Geneva Medical School, Geneva, Switzerland.

B5, B8, D8 Courtesy of Drs. Bradley Schulte, Department of Pathology, Medical School of South Carolina, Charleston, SC, and Jonathan Parsons, Department of Anatomy, Medical School, University of Minnesota, Minneapolis, MN.

B6, B9, C1, C3, C4 Courtesy of Dr. Damon C. Herbert, Department of Anatomy, The University of Texas Health Science Center at San Antonio, San Antonio, TX.

B7 Courtesy of Dr. Li J. Yuan, University of Claude-Bernard, Lyon, France.

C2 Courtesy of Dr. Gwen Childs Moriarty, Department of Anatomy, University of Texas Medical Branch, Galveston, TX.

C6 Courtesy of Dr. Masataka Shiino, Department of Anatomy, Wakayama Medical College, Wakayama, Japan.

C9 Courtesy of Dr. Ann Judith Silverman, Department of Anatomy, Columbia University, College of Physicians and Surgeons, New York, NY.

D3, E5, E6 Courtesy of Dr. Peter Gould, The Middlesex Hospital Medical School, London, England.

D5 Courtesy of Dr. Hisao Fujita, Department of Anatomy, Hiroshima University School of Medicine, Hiroshima, Japan.

D7 Courtesy of Dr. Bruce K. Wetzel, National Institutes of Health, Bethesda, MD.

E1 Courtesy of Dr. J. Tepperman, Department of Pharmacology, College of Medicine, State University of New York, Syracuse, NY.

E4 Courtesy of Dr. Sanford Roth, Department of Pathology, School of Medicine, Northwestern University, Chicago, IL.

F2 Courtesy of Dr. Virginia Black, Department of Cell Biology, New York University School of Medicine, New York, NY.

F4, F8 Reproduced with permission from J. A. G. Rhodin, Journal of Ultrastructural Research 34:31, 1971.

F5, F6, F9 Courtesy of Dr. John A. Long, Department of Anatomy, School of Medicine, University of California, San Francisco, CA.

G2 Reproduced with permission from Odile Grynszpan-Winograd, *Handbook of Physiology*, Section 7, Vol. 6, American Physiological Society, Bethesda, MD, 1975.

G6 Reproduced with permission from Lars-Inge Larsson, Diabetologia 12:233, 1976.

G8 Courtesy of Dr. Robin Michaels, Department of Physiology and Biophysics, Washington University School of Medicine, St. Louis, MO.

A1 Diagram of major vessels entering and leaving liver. The relationship of the sinusoids and hepatic lobules to these vessels is shown at left.

A2 Diagram illustrating relationship of hepatic lobule to portal canal and to hepatic vein.

A3 LM of liver showing relationship between central vein and portal canal. Observe the radial arrangement of cells emanating from the central vein. (H & E)

A4 SEM of liver illustrating radial arrangement of cells from central vein toward portal canal. CV, central vein; PV, portal vein.

A5 Diagram of hepatic lobule showing flow of blood from portal triads to central vein and flow of bile from canaliculi in liver cords to bile ducts in portal triad.

A6 Diagram depicting flow of blood in classical hepatic lobule. Blood flows centripetally from portal triads to central vein in center of hepatic lobule.

A7 Diagram of Rappaport's lobule, called the liver acinus. Those cells within the hepatic lobule that are supplied by branches from one or two adjacent portal triads constitute the hepatic lobule of Rappaport. In this model, cells at the periphery of the (classical) lobule are exposed to higher concentrations of oxygen and nutrients, whereas those closest to the central vein are exposed to lower concentrations of these materials.

A8 LM of portal triad. The portal vein (center) has a large branch (left), from which several smaller branches extend, feeding sinusoids between plates of liver cells. Also present within the triad are branches of the hepatic artery and the bile duct. (H & E)

A9 Higher-magnification LM of portal triad illustrating branches of portal vein, hepatic artery, and bile duct. (H & E)

B1 LM of central vein of liver lobule. Hepatocytes adjacent to the central vein contain abundant amounts of lipofuscin pigment. Sinusoids can be seen (top) emptying into the central vein. (H & E)

B2 SEM of liver showing central vein and openings of sinusoids into lumen of vein.

B3 High-magnification LM of liver parenchyma. Note the cordlike arrangements of hepatocytes separated by liver sinusoids. (H & E)

B4 TEM of liver parenchyma showing relationships of hepatocytes to liver sinusoid. Observe the numerous mitochondria. The plasmalemma of the hepatocyte exposed to the sinusoids has microvilli as surface specializations, whereas the plasmalemma of the hepatocyte abutting on other hepatocytes has tight junctions, gap junctions, and microvilli. This tissue was taken from a starved rat and, therefore, the hepatocytes are depleted of glycogen.

B5 TEM of hepatocytes from a fed rat, illustrating accumulation of particulate glycogen within cytoplasm. Bile canaliculi can be seen between adjacent hepatocytes.

B6 TEM of hepatocyte at higher magnification, revealing abundant rough endoplasmic reticulum, particulate glycogen, and mitochondria.

B7 TEM autoradiograph of rat liver perfused 15 minutes after injection of 125I-labeled beta glucuronidase. Autoradiograph grains representing the localization of this enzyme are found overlying endothelial cells and Kupffer cells lining the sinusoidal lumen, but not over hepatocytes. This illustrates the presence of specific receptors for lysosomal enzymes within the cell types lining the sinusoidal lumen, but not within the hepatocytes.

B8 TEM of radiograph of liver perfused after injection with ^{125}I-labeled glucagon. Autoradiographic grains representing the localization of glucagon are now found over the periphery of hepatocytes but not over endothelial cells or Kupffer cells lining the sinusoidal lumen.

B9 Higher-magnification TEM of same tissues seen in B8, revealing localization of silver grains representing glucagon over plasmalemma of hepatocytes. Liver cells are known to contain specific receptors for glucagon, whereas the cells lining the sinusoidal lumen do not. Identify the space of Disse.

C1 Diagram representing flow of bile and portal triad.

C2 High-magnification LM of liver cords and adjacent sinusoids. Two liver cells (center) abut one another and contain a small bile canaliculus at their interface. Gold brown lipofuscin pigment is seen in most of these cells. (H & E)

C3 High-magnification LM of liver. Two cells (center), one of which (on the right) is binucleate, have a bile canaliculus at their interface. (azo-carmine stain)

C4 SEM of fractured liver revealing sinusoid (left) and fractured liver cell surfaces (right). The bile canaliculi can be seen on the surface of fractured hepatocytes and contain small microvilli. The luminal surface of the sinusoid possesses both fenestrations and large perforations. The hepatocyte's surface facing the sinusoidal lumen is covered by a series of microvilli.

C5 TEM of interface between two hepatocytes showing bile canaliculus. The luminal surface of the canaliculus contains numerous microvilli and is sealed from the lateral intercellular space by zonula occludens at both margins. Observe the presence of Golgi and pericanalicular dense bodies.

C6 TEM illustrating transition between bile canaliculi and terminal bile ductule in portal triad. The inset (lower left) shows a one-micron section of a portal area and similar transition. PV, portal vein; HA, hepatic artery, BD, bile ductules.

C7 High-magnification LM of rat liver after intravenous injection of trypan blue. This dye has been phagocytosed by Kupffer cells lining the sinusoids. (H & E)

C8 TEM of rat liver showing Kupffer cell spanning sinusoidal lumen. This cell has very short cytoplasmic extensions.

C9 TEM of liver sinusoid illustrating presence of Kupffer cell (far right). This tissue has been processed for peroxidase activity. The enzyme peroxidase is found within Kupffer cells and macrophages but not within endothelial cells, an example of which is seen at far left.

D1 SEM of fractured surface of liver sinusoids. Kupffer cells can be seen spanning the sinusoidal lumen at left and right. K, Kupffer cells; S, sinusoidal lumen; En, endothelial cell; BC, bile canaliculus; LP, liver plate.

D2 TEM of liver sinusoid showing morphology of lipocytes. These cells store lipids and are rich in vitamin A.

D3 Low-magnification LM showing pronounced folding of gallbladder mucosa. (H & E)

D4 SEM of gallbladder mucosal surface. Compare the numerous folds, or rugae, on the surface with those seen by light microscopy in D3.

D5 High-magnification LM of gallbladder mucosa. The epithelium consists of simple columnar cells with a well-developed microvillous border. The lamina propria is rich in blood vessels and contains connective tissue fibers. (H & E)

D6 TEM of gallbladder showing morphology during active water transport (right) and in inactive stage (left). Note the increased intercellular space in the epithelium during the active transport of water.

D7-D9 Blank

E1 Diagram of gastrointestinal tract and accessory organs of digestion.

E2 Diagram of overall histological organization of digestive tract from esophagus through large intestine. The wall of the digestive tract consists of four layers; named in order from the lumen outward, these are the mucosa, the submucosa, the muscularis, and the adventitia. The mucosa has three components: a superficial epithelium, an underlying connective tissue stroma, and a relatively thin layer of smooth muscle called the muscularis mucosa.

E3 Macrophotograph of longitudinal and cross sections of esophagus. Observe the star-shaped lumen in the latter section, as well as the presence of different layers in the wall. (H & E)

E4 Low-magnification LM illustrating the four layers of the esophagus. From right to left, these consist of (1) the mucosa, made up of epithelium, underlying lamina propria, and muscularis mucosa; (2) the submucosa, containing two mucous glands; (3) the muscularis, consisting of inner circular and outer longitudinal layers of smooth muscle; and (4) a portion of adventitia (upper left). (H & E)

E5 Higher-magnification LM of mucosa and submucosa of esophagus. The esophageal glands are located in the submucosa and are involved in the production of mucus for the lubrication of food during swallowing. (H & E)

E6 LM showing esophageal-cardiac junction. Note the stratified squamous nonkeratinizing epithelium of the esophagus (right) and the simple columnar epithelium of the stomach (left), which is folded into invaginations called cardiac glands. (H & E)

E7 High-magnification LM of junction between epithelium of esophagus and that of cardiac region of stomach. (H & E)

E8-E9 Blank

F1 Macrophotograph of luminal surface of esophagus and stomach. The esophagus is connected to the cardiac region of the stomach (upper left). Rugae, or folds, of the mucosal surface extend throughout the body, fundus, and down into the pylorus (lower left). The thickening of smooth muscle (lower left) is called the pyloric sphincter.

F2 Diagram showing subdivisions of stomach wall and cytological details of gastric glands in body-fundus of stomach.

F3 LM illustrating cardiac region of stomach. Observe the shallow gastric pits and the short cardiac glands. (H & E)

F4 Low-magnification LM of body of stomach, illustrating presence of gastric glands. Observe the longer gastric pits and the presence of acidophilic and basophilic regions within the gastric glands. The muscularis mucosa separates the gastric glands from the underlying submucosa. (H & E)

F5 High-magnification LM of base of gastric pit and its junction with neck of gastric gland. Surface mucous cells can be seen lining the gastric pits, whereas the necks of the gastric glands consist of parietal cells and intervening mucous neck cells. (H & E)

F6 SEM of body of mouse stomach. Observe the tubular glands and openings of gastric pits in the mucosal surface.

F7 LM illustrating middle and basal portions of gastric glands. Notice the predominance of parietal cells in the body of the gland, and the larger number of basophilic chief cells in the base of the gland. (H & E)

F8 High-magnification LM of body of gastric gland. Acidophilic parietal cells can be seen bulging from the lateral surface of the gastric gland. The small narrowed apex of these cells opens to the lumen of the gland. (H & E)

F9 Diagram illustrating structure of parietal cell and mechanisms involved in formation of hydrochloric acid.

G1 TEM of parietal cell in gastric gland. Observe the well-developed intracellular canaliculi in this cell, which is active in the formation of hydrochloric acid. Go, Golgi; Nu, nucleus; Fc, fibroblast; m, mitochondria; Ly, lysosomes; Ld, lipid droplet; Jc, junctional complex; Cc, chief cell.

G2 TEM of parietal cell. It is not involved in the secretion of hydrochloric acid. The intracellular canaliculi have lost their contact with the lumen of the gland. The large numbers of microvilli in the canaliculi have been internalized by an endocytic mechanism, and in this way extra surface membrane is stored within the cell. Upon stimulation, the stored membrane will fuse again with the cell surface and reform the intracellular canaliculi.

G3 TEM showing immunocytochemical localization of intrinsic factor within the parietal cell. Specific staining for intrinsic factor can be seen within tubulo-vesicles in the cytoplasm. N, nucleus; G, Golgi; RER, rough endoplasmic reticulum.

G4 Low-power TEM of gastric gland illustrating organization of chief cells within basal region of the gland.

G5 TEM of a chief cell showing its exocrine organization. In the stomach the chief cell is involved in the formation of rennin, pepsinogen, and gastric lipase.

G6 Low-power LM of pyloric mucosa. Note the long gastric pits and the highly coiled pyloric glands. (H & E)

G7 Immunofluorescence localization of gastrin at LM level within pyloric glands. Observe the highly fluorescent cell in the gastric gland (center). Note the orientation of the immunofluorescence toward the lamina propria, or connective-tissue surface of the gland.

G8 TEM of pyloric gland showing ultrastructure of G cell, or gastrin-producing cell. Observe the basal polarization of secretory granules containing gastrin toward the connective-tissue surface of the cell. Mg, mucous granule; Glu, gland lumen; Mv, microvilli; Go, Golgi; m, mitochondria; N, nucleus; Er, endoplasmic reticulum.

G9 TEM of pyloric gland showing morphology of enterochromaffin cell, which contains serotonin. Like other endocrine cell types within the mucosa, the granules are polarized in the base of the cell in order to be released into the connective tissue, lamina propria, where their contents will diffuse into the peripheral circulation.

Acknowledgments

A1 Reproduced with permission from A. D. Hally and Sybil M. Lloyd, *Clinical Science*, Biochemical Society, London, England, 1968.

A4, C4 Reproduced with permission from Tsuneo Fujita, *SEM Atlas of Cells and Tissues*, T. Fujita, K. Tanaka, and J. Tokunaga, editors, Igaku-Shoin, Tokyo, Japan, 1981.

B4, B7, C8 Courtesy of Dr. Ann L. Hubbard, Department of Cell Biology and Anatomy, Johns Hopkins School of Medicine, Baltimore, MD.

B5, B6 Reproduced with permission from H. D. Fahimi, Laboratory Investigation 16:736, 1967.

B8, B9 Courtesy of Dr. Victoria Iwanji, Genetics and Cell Biology, University of Minnesota, St. Paul, MN.

C5 Courtesy of Dr. Richard Wood, Department of Anatomy, University of Southern California School of Medicine, Los Angeles, CA.

C6 Reproduced with permission from Richard Wood, *Bailey's Textbook of Histology*, 17th edition, W. M. Copenhaver, D. E. Kelly, and R. L. Wood, editors, Williams and Wilkins, Baltimore, MD, 1978.

C9 Reproduced with permission from H. D. Fahimi, American Journal of Pathology 80:349, 1975.

D1 Reproduced with permission from P. M. Motta, *The Liver. An Atlas of SEM*, P. M. Motta, M. Muto, and T. Fujita, editors, Igaku-Shoin, Tokyo, Japan, 1978.

D2 Courtesy of Dr. H. D. Fahimi, Institute of Anatomy, University of Heidelberg, Heidelberg, Germany.

D6 Reproduced with permission from Gordon Kaye, Journal of Cell Biology 30:237, 1966.

E2 Reproduced with permission from Donald W. Fawcett, *A Textbook of Histology*, 10th edition, W. Bloom and D. W. Fawcett, editors, Saunders, Philadelphia, PA, 1975.

F1 Reproduced with permission from Chihiro Yokochi, *Photographic Anatomy of the Human Body*, C. Yokochi, editor, Igaku-Shoin, Tokyo, Japan, 1969.

F9 Reproduced with permission from A. D. Hally and Sybil M. Lloyd, *A Companion to Medical Studies*, R. Passmore, editor, Blackwell Scientific Publications, Oxford, England, 1968.

G1, G8 Reproduced with permission from Tatsuo Ebe and S. Kobayashi, *Fine Structure of Human Cells and Tissues*, T. Ebe and S. Kobayashi, editors, Igaku-Shoin, Tokyo, Japan, 1972.

G2 Courtesy of Dr. Susumu Ito, Department of Anatomy, Harvard Medical School, Boston, MA.

G3 Courtesy of Dr. Joel S. Levine, Department of Pathology, University of Colorado, Denver, CO.

G4 Courtesy of Dr. Herbert Helander, Department of Anatomy, University of Umea, Umea, Sweden.

G5 Reproduced with permission from Walter Rubin, Laboratory Investigation 19:598, 1968.

G7 Courtesy of Dr. Juan Lechago, Department of Pathology, UCLA School of Medicine, Torrance, CA.

G9 Reproduced with permission from Walter Rubin, Journal of Cell Biology 50:403, 1971.

FICHE 11

A1 Low-magnification LM of pyloric-duodenal junction. Tracing the pyloric mucosa (left) over the pyloric sphincter, one can observe the formation of villi within the duodenal mucosa and the appearance of Brunner's glands in the submucosa down to the muscularis mucosa. (H & E)

A2 SEM of pyloric-duodenal junction showing flattened surface of pyloric mucosa (left) and evaginations, or villi, in duodenal mucosa, which are located beyond the pyloric sphincter.

A3 Diagram illustrating structure of small and large intestines.

A4 Diagram of crypt and villus epithelium within small intestine, and of types of epithelial cells, their location and function.

A5 Low-magnification LM of duodenal mucosa. Easily distinguished are the numerous fingerlike villi, the glandular invaginations called the intestinal crypts of Lieberkuhn, and, beneath the muscularis mucosa, the mucus-secreting Brunner's glands. (H & E)

A6 High-magnification LM of base of intestinal crypts of Lieberkuhn and their interface with mucus-secreting Brunner's glands. Ductular extensions of Brunner's glands empty into the base of the intestinal crypts. (H & E)

A7 High-magnification LM of tip of intestinal villus. Cells are desquamating, or being lost, from the surface of the villus. (H & E)

A8 SEM of surface of intestinal villus. The villus is similar to that seen in A7. Notice that cells undergoing desquamation project above the rest of the epithelial surface.

A9 Side view of intestinal villus by SEM, showing furrows, or contraction bands, formed during fixation of the tissue. These bands are formed when smooth muscle contracts within the lamina propria of the villus.

B1 High-magnification LM of epithelium of two adjacent villi. Observe the pale-staining goblet cell (center). Several lymphocytes can also be seen traversing the epithelium.

B2 TEM of villus epithelium. Notice the goblet cell (center), also, numerous lymphocytes can be seen within the epithelium. In the lamina propria a fenestrated capillary is seen at the base of the goblet cell.

B3 High-magnification TEM of absorptive epithelial cells, revealing extensive microvilli on apical surface and presence of glycocalyx, which contains enzymes involved in digestion of disaccharides and small peptides.

B4 TEM using ferritin-labeled antibodies to demonstrate localization of sucrase in microvillous border of intestinal epithelial cells.

B5 FF of junctional complex found at apical surface of absorptive epithelial cells. The extensive zonula occludens seen in this micrograph illustrates the permeability barrier that exists between the intestinal lumen and the intercellular space beneath the junctional complex.

B6 Diagram depicting absorption of nutrients across microvillous border of intestinal epithelial cells.

B7 LM of ileal mucosa revealing presence of lacteals within intestinal villi. (H & E)

B8 High-magnification of intestinal villus showing presence of lacteal within lamina propria. Compare the lacteal with the small venule (right). (H & E)

B9 SEM of ileal mucosa. Note the leaf-shaped villi and, on floor of intestine, openings of intestinal crypts of Lieberkuhn.

C1 LM of ileal mucosa. Observe the large number of goblet cells within the epithelium and the presence of acidophilic Paneth cells at the base of the intestinal crypts. The muscularis mucosa is seen immediately beneath the intestinal glands. (H & E)

C2 LM of frozen section of ileum immunocytochemically stained for the neurotransmitter VIP. Observe the plexus of nerve fibers surrounding the apical portion of the crypts and extending up into the villus to just beneath the epithelium.

C3 Immunocytochemical demonstration (LM) of lysozyme within Paneth cells in rat ileum. Observe cells containing lysozyme, within the lamina propria, which are either polymorphonuclear cells or macrophages.

C4 High-magnification LM of base of intestinal crypts revealing presence of Paneth cells. Note the extensive number of acidophilic secretory granules (containing lysozyme) in the apex of these cells. (H & E)

C5 TEM of base of intestinal crypt containing large numbers of Paneth cells in rat ileum. The Paneth cells are serous cells which secrete lysozyme, a bactericidal enzyme. These cells also contain an extensive lysosomal apparatus and are capable of endocytosis of microorganisms found within the crypt lumen. Two examples of enteroendocrine cells are also visible.

C6 LM of intestinal crypts of Lieberkuhn in the mouse after injection of tritiated thymidine. Stem cells in the base of the intestinal crypts incorporate tritiated thymidine and continue to divide to give rise to cells that will migrate up the intestinal crypt and eventually onto the villus. (PAS hematoxylin)

C7 High-magnification LM of lamina propria within intestinal villus. observe the large number of plasma cells within the lamina propria. (H & E)

C8 TEM of plasma cells within lamina propria. A lacteal can be seen (far left). These plasma cells within the intestine are involved in the production of secretory IgA, an immunoglobulin that is transported across the epithelium into the intestinal lumen.

C9 LM of section of intestine stained immunocytochemically for localization of secretory IgA. Large numbers of dark-staining plasma cells can be seen within the lamina propria of intestinal villi and also within the submucosa. The apical portions of the cells of the intestinal crypts of Lieberkuhn are also stained for secretory IgA, for it is these epithelial cells that are involved in the transport of this immunoglobulin from the lamina propria into the lumen of the intestine.

D1 Diagram showing synthesis, transport, and secretion of secretory IgA in intestinal mucosa.

D2 Diagram of relationship between antigen transport, maturation of plasmablasts, and their migration to mucosal surfaces.

D3 TEM of crypt of Lieberkuhn in duodenum. A variety of endocrine cells are visible in the epithelium. Each of these cells is involved in the elaboration of a distinct intestinal hormone. The granules are polarized in the base of the cell, where their secretion will be released into the lamina propria. Undifferentiated crypt cells in the intestine contain large granules near the lumen of the gland and may be involved in the epithelial transport of secretory IgA. Lu, lumen; Go, Golgi complex; m, mitochondria; R, rough ER; f, cytoplasmic filaments; Bl, basal lamina; Ec, enterochromaffin cell; D, type of enteroendocrine cell; L, type of enteroendocrine cell.

D4 Macrophotograph of intestine showing plicae circulares as transverse folds.

D5 LM illustrating cross section of individual plica circulares. The submucosa extends up into the fold, and extensive amounts of lymphoid tissue can be seen within both the submucosa and lamina propria. (H & E)

D6 LM of rat ileum illustrating presence of Peyer's patches. Because of the accumulation of lymphoid tissue beneath the epithelium, intestinal villi are absent in the region of Peyer's patches. Lacteals can also be seen within a number of villi. (H & E)

D7 High-magnification LM of epithelium overlying dome of Peyer's patch. Specialized cells called M cells are present within this epithelium but are not easily distinguished by light microscopy. (H & E)

D8 SEM of Peyer's patch in rat ileum. Observe the dome-shaped epithelium over the Peyer's patch and the presence of intestinal villi around the margin of the patch.

D9 High-magnification TEM of intestinal epithelium overlying a Peyer's patch 30 minutes after introduction of horseradish peroxidase into intestinal lumen. Reaction product indicating the presence of the horseradish peroxidase enzyme can be seen (upper right) surrounding intestinal microvilli. Reaction product also fills vesicles and tubules within the M cell but not the columnar cells seen on either side of this cell type. Two lymphocytes in the extracellular space indent the M cell from the left. Only the M cell in the overlying epithelium on the Peyer's patch appears to be involved in the transport of markers such as horseradish peroxidase from the intestinal lumen into the underlying tissue. The strategic location of this cell type within this epithelium and its association with lymphoid follicles suggest that it may play a role in transporting antigenic material from the intestinal lumen to the underlying lymphocytes within the lamina propria. M, M cell; C, columnar cells; L, lymphocytes; G, Golgi.

E1 SEM of ileocecal junction. Intestinal villi can be seen (left) protruding into the intestinal lumen. Running diagonally across this frame is the junction between ileal epithelium and colonic epithelium which consists of a flattened surface without any evaginations.

E2 LM of appendix in cross section. Observe the detritus within the lumen and the presence of lymphoid follicles within the lamina propria and submucosa. (H & E)

E3 Higher-magnification LM of mucosa within appendix. Intestinal villi are absent; however, crypts of Lieberkuhn can be seen projecting into the underlying connective tissue, the lamina propria. Lymphatic nodules are present within both the lamina propria and the submucosa. (H & E)

E4 Low-magnification LM of large intestine. Notice the lack of villar projections within the mucosal surface, the relatively thick submucosa, and the thickened muscularis seen in the outer wall. (H & E)

E5 LM of mucosa and submucosal layers of large intestine. The mucosa consists of tightly packed crypts of Lieberkuhn abutting on the muscularis mucosa. Within the submucosa, large dilated veins characteristic of this region of the intestine can be seen. A portion of the muscularis layer is visible at the bottom of the frame. (H & E)

E6 LM of colonic mucosa. Observe the large number of goblet cells present within the crypts of Lieberkuhn. Numerous lymphocytes are present within the lamina propria, the muscularis mucosa, and the submucosa. (H & E)

E7 Higher-magnification LM of colonic epithelium. Owing to the large number of lymphocytes and leukocytes present within the lamina propria and also within the epithelium, the gastrointestinal tract is considered to be a site of chronic inflammation. (H & E)

E8 TEM of colonic mucosa illustrating structure of goblet cells within surface epithelium. Large mucin droplets can be seen within these cells, and one of the cells is discharging mucus into the intestinal lumen.

E9 SEM of surface of colonic mucosa. Note the openings of the crypts of Lieberkuhn onto the surface, and the presence of a mucus discharge (center). The lateral margins of the surface epithelial cells are easily distinguished, as are the openings of several goblet cells within the mucosa.

F1 Diagram of conducting and respiratory portions of respiratory tract. Shown at increasing magnifications are the respiratory portion of the lung, two alveoli, and details of the blood-air barrier.

F2 Macrophotograph of epiglottis showing both esophageal and laryngeal surfaces. Observe the dark-staining cartilage and the presence of lymphoid follicles. (H & E)

F3 LM of epithelial junction between stratified squamous epithelium on esophagus and pseudostratified columnar epithelium characteristic of respiratory tract. An oblique section of a taste bud is also seen. (H & E)

F4 Endoscopic views of vocal cords within larynx. By changes in the position of the laryngeal cartilages, the rima glottidis, or opening, between the vocal cords can be opened or closed. The left photo illustrates the vocal cords at rest, i.e., when we breathe but do not speak. They are then relaxed, and the rima glottidis is wide open. The right photo shows the vocal cords, which appear white, stretched in the glottis, now closed. During speech, the stretched vocal cords form a narrow opening through which air is forced. The pitch of the sound emitted corresponds to the degree of vibration of the vocal cords.

F5 Macrophotograph of laryngeal epithelium showing both false and true vocal cords. Between the false vocal cords, or vestibular folds, and the true vocal cords the opening of the laryngeal sacule can be seen. Large numbers of seromucous glands are present within the vestibular fold; within the vocal cord one can see the fibroelastic connective tissue underlying the epithelium. The vocalis muscle, part of the thyroarytenoid, is deep to the fibroelastic connective tissue. (H & E)

F6 LM of vestibular fold and true vocal cord. Observe the presence of glands within the former, and fibroelastic connective tissue within the latter. Note also that each fold is covered by a distinct type of epithelium. (H & E)

F7 Macrophotographs of mucosal surface of trachea (left) and of trachea viewed at origin of the two bronchi (right). The trachea is a tube, approximately four inches long and a little less than an inch in diameter, whose lumen is maintained in a patent configuraton by the presence of some 16 to 20 incomplete cartilaginous rings. In this field of view at least five of these cartilages can be seen. Extending into the lungs, the primary bronchi (right) are approximately one cm wide and branch to form the bronchial tree, the smallest subdivisions of which are the respiratory bronchioles. Like the trachea, the primary bronchi are kept open by cartilaginous rings, and the branch point is strengthened by a larger, specially formed cartilaginous ring.

F8 Macrophotograph of larynx and esophagus. Observe the presence of cartilage within the tracheal wall and the incomplete nature of the ring seen at lower right. The esophagus lies more posteriorally, and in this field of view is characterized by a star-shaped lumen. (H & E)

F9 LM of tracheal wall. Observe the pseudostratified columnar epithelium characteristic of the respiratory tract, underlying fibroelastic tissue, small seromucous glands, and a portion of the cartilaginous ring.

G1 SEM of fracture of tracheal wall. Compare with F9, observing the location of the pseudostratified columnar epithelium, underlying fibroelastic tissue, and a portion of the cartilaginous ring.

G2 High-magnification LM of pseudostratified columnar epithelium of trachea. A variety of cell types can be found within the tracheal epithelium, including mucous cells, ciliated cells, basal cells involved in the mitotic renewal of this epithelium, endocrine cells containing secretory granules polarized toward the lamina propria, and nonciliated cells containing an extensive microvillous border. The basement membrane of the epithelium is easily seen and separates the epithelium from the underlying lamina propria, which consists of a loose connective tissue with interwoven collagenous and elastic fibers. (H & E)

G3 SEM of trachial epithelium. Dome-shaped cells indicate the sites of secretory activity. Note the appearance of cilia and microvilli in surrounding cells and the presence of capillaries within the lamina propria.

G4 TEM of tracheal epithelium. Examples of ciliated cells, basal cells, endocrine cells, and cells possessing a microvillous border can be distinguished. Inset LM (lower right) illustrates staining for hormones within the endocrine cell, which is outlined in black in the center of the field. Lu, lumen; Ci, ciliated cells; Ba, basal cell; K, endocrine cell; Go, goblet cell.

G5 Higher-magnification SEM of tracheal epithelial surface. Observe the presence of ciliated cells and cells possessing microvilli. The presence of craterlike structures in the surface of some of the cells suggests possible secretory activity. A higher density of microvilli is seen near the lateral margin of cells, thus outlining their borders.

G6 LM of cartilaginous bronchiole in lung. Small portions of hyaline cartilage can be seen beneath the mucosal surface. Substantial amounts of lymphoid tissue are also present. (H & E)

G7 LM of muscular bronchiole in lung. The smooth muscle encircling the epithelium of the bronchiole plays an important role in regulating the diameter of the bronchiole. (H & E)

G8 TEM of bronchiolar epithelium showing protrusion of Clara cell into lumen. Note the ciliated cell (left).

G9 LM of bronchiolar epithelium illustrating presence of clusters of macrophages on luminal surface of epithelium. (colloidal iron and Ponceau counterstain)

Acknowledgments

B2, C8 Courtesy of Dr. David G. Chase, Cell Biology Research Laboratory, Veteran's Administration Hospital, Sepulveda, CA.

B3 Reproduced with permission from Susumu Ito, *The Cell*, 2d edition, D. W. Fawcett, editor, Saunders, Philadelphia, PA, 1981.

B4 Courtesy of Dr. R. Gitzelmann, Division of Metabolism, University Pediatric Department, Kinderspital, Zurich, Switzerland.

B5 Reproduced with permission from Adolfo Martinez-Palomo, *Electron Microscopy*, 1978, Ninth International Congress on Electron Microscopy, Vol. 3, Microscopical Society of Canada, Toronto, Canada, 1978.

C2 Reproduced with permission from Tomas Hokfelt and Marianne Schultzberg, Nature, Vol. 284, Macmillan Journals, London, England, April 1980.

C6 Courtesy of Drs. Hazel Cheng and Matt Bjerknes, Department of Anatomy, University of Toronto Medical School, Toronto, Canada.

D3 Reproduced with permission from Shigeru Kobayashi, Archivum Histologicum Japonicum 31:477, 1970.

D4 Reproduced with permission from Chihiro Yokochi, *Photographic Anatomy of the Human Body*, C. Yokochi, editor, Igaku-Shoin, Tokyo, Japan, 1969.

D8, D9 Courtesy of Dr. Robert L. Owen, Department of Medicine, Veteran's Administration Hospital, San Francisco, CA.

E8 Courtesy of Dr. Marian Neutra, Department of Anatomy, Harvard Medical School, Boston, MA.

F4, F7 Reproduced with permission from Lennart Nilsson, *Behold Man*, Little, Brown, Boston, MA, 1973.

G4 Reproduced with permission from Ernest Cutz, Cell and Tissue Research 158:425, 1975.

G8 Courtesy of Dr. Charles Kuhn III, Department of Pathology, Washington University School of Medicine, St. Louis, MO.

G9 Reproduced with permission from Sergei P. Sorokin, Anatomical Record 181:607, 1975.

A1 Diagram of respiratory subdivisions in lung. Respiratory bronchiole, alveolar duct, alveolar sac, and alveoli can be seen.

A2 LM of respiratory bronchiole in lung. Observe the changes in the epithelium in the transition from terminal bronchiole to respiratory bronchiole shown in this frame. Note the openings of the alveoli. (H & E)

A3 Low-magnification LM of lung. Compare with A1 and find examples of respiratory bronchiole, alveolar duct, atrium, alveolar sac, and alveoli. (H & E)

A4 SEM of terminal and respiratory bronchioles within rat lung. The respiratory bronchiole can be recognized by the openings of alveoli.

A5 SEM of atrium and alveolar sac within rat lung.

A6 LM of two adjacent alveoli in lung. Locate capillaries. What are the epithelial components of the alveolar wall? (H & E)

A7 SEM of an alveolus in rat lung. Capillary loops can be seen in relief beneath the epithelium lining the alveolar surface. Examples of alveolar pores are also visible.

A8 High-magnification LM of alveolar wall in lung. Type II alveolar cells can be seen (far left and upper right) as well as a macrophage attached to the luminal surface of type I epithelial cells (lower left). The morphology of endothelial cells and type I cells is difficult to distinguish by LM even at this high magnification. (H & E)

A9 TEM of interalveolar wall. Note the thickness of alveolar wall and the route gas molecules must transverse to move from red blood cell to alveolar space and vice versa. A, alveolar space; BM, basement membrane; C, capillary lumen; EP , type I epithelial cell; EP , type II epithelial cell; and FB, fibroblast.

B1 Diagram of secretory processes of the great alveolar, or type II, epithelial cell in lung.

B2 TEM of alveolar wall. It is composed of epithelium, capillaries, and connective tissue elements. The alveolar epithelium consists of two types of cells: the squamous alveolar epithelial cell, or type I cell, extends thin cytoplasmic processes over the capillary wall, and the great alveolar epithelial cell, or type II cell, is characterized by the presence of lamellar bodies containing surfactant. In many locations the basement membrane of the epithelial cells fuses into one layer with the respective basement membrane of the capillaries. Gaseous exchange between the blood and the air is believed to occur through the attenuated cytoplasm

of the squamous alveolar epithelial cell, or type I cell, the fused alveolar basement membrane, and the attenuated cytoplasm of the capillary endothelial cell. Alu, alveolar lumen; Am, fused basement membranes of epithelial and endothelial cells; Ed, endothelial cell; F, fibrocyte; R, erythrocyte; Cap, capillary; Sc, squamous alveolar epithelial cell; Gc, great alveolar, or type II, epithelial cell; Lb, lamellar bodies; Cf, collagenous fibers; Ef, elastic fibers.

B3 TEM of great alveolar, or type II, epithelial cell in rat lung. The type II cell is larger than adjacent type I cells and contains large numbers of lamellar bodies, which are thought to contain surfactant. AL, alveolar lumen; Mv, microvilli; MVB, multivesicular body; LB, lamellar body; CL, capillary lumen; BL, fused basement membranes of the endothelial cell and type II cell; M, mitochondria.

B4 LM of lung showing alveolar pore (top center). Compare with A3 and B5. (H & E)

B5 SEM of alveolus in rat lung. Examination of the epithelial surface of this alveolus reveals the presence of capillary loops beneath the epithelium and of alveolar pores.

B6 TEM of alveolar pore showing leukocytes passing from one alveolar space into adjacent alveolar space.

B7 Diagram of pulmonary macrophage functions.

B8 TEM of alveolar macrophage washed from lungs of a normal, nonsmoking subject.

B9 TEM of alveolar macrophage from lungs of a normal, tobacco-smoking subject. Note the large number of residual bodies with myelin figures.

C1 Diagram of hemisection of kidney, revealing renal pelvis and arterial supply to renal cortex and medulla.

C2 Schematic cutaway of renal pyramid and overlying renal cortex, showing interrelationships between medullary rays and the arterial blood supply to cortex and medulla.

C3 Macrophotograph of monkey kidney. Observe the medulla and cortical relationships. Medullary rays are easily seen, as well as arcuate vessels passing between medulla and cortex. Renal vessels and the ureter are also visible (far left). (H & E)

C4 LM of corticomedullary junction. Several renal corpuscles and a medullary ray can be seen within the cortex. Portions of collecting tubules and vasa recta are present within the medulla. (H & E)

C5 LM of kidney cortex showing interlobular artery, renal corpuscle surrounded by convoluted tubules, and medullary ray. (H & E)

C6 SEM of vascular cast of rat kidney. The interlobular artery is easily seen, and its branches, which are the afferent arterioles, supply numerous glomeruli with blood.

C7 Diagram of renal corpuscle and juxtaglomerular apparatus within nephron.

C8 LM illustrating both vascular and urinary poles of renal corpuscle. Examine the parietal and visceral layer of Bowman's capsule; the latter surrounds the capillary tufts. (H & E)

C9 TEM of renal corpuscle at low magnification. Compare with C7, locating the parietal and visceral layers of Bowman's capsule, endothelial cells, and red blood cells.

D1 LM of renal corpuscle in kidney. Find examples of the visceral epithelium (or podocytes), endothelial cells, basement membrane, red blood cells, and parietal layer of Bowman's capsule. (H & E)

D2 TEM of renal corpuscle showing both parietal and visceral epithelial layers. Contrast the morphology of these two epithelial cell types. Note also the thickness of the glomerular filtration barrier. Several red blood cells and a platelet can be seen within the capillary lumen.

D3 SEM of glomerulus in which several capillaries have been fractured, thus revealing their internal surface. The processes of podocytes can be seen covering the capillary loops, whereas the fractured surface shows the fenestrations within the endothelial cells.

D4 TEM of glomerular capillary and surrounding visceral epithelial cell, or podocyte. Unlike other fenestrated capillaries, the fenestrae within the glomerular capillaries lack diaphragms. The basal lamina of the endothelial cell and podocyte appear to be fused in this frame. The adjacent foot processes of the podocyte abut the basal lamina and are interconnected by slit diaphragms such as those seen at the arrow. US, urinary space; Ep, epithelial cell, or podocyte; fp, foot process; B, fused basal laminae of the endothelial cell and podocyte; f, fenestrae; En, endothelial cell; Cap, capillary lumen; RBC, red blood cell.

D5 SEM of internal surface of glomerular capillary. Compare the morphology by SEM to that seen by TEM in D4. Note the appearance of the fenestrae within the endothelial cell and the foot processes of the podocyte.

D6 High-magnification SEM of glomerular capillary. Again, note the presence of the fenestrae, the location of the basement membrane (indicated by the letter B), and the foot processes of the podocyte.

D7 SEM of glomerular capillary loops in kidney. The podocyte extends both primary and secondary rami which envelop as foot processes the surfaces of the capillary loops.

D8 High-magnification TEM of glomerular filtration barrier. A red blood cell can be seen within the capillary lumen. The basement membrane consists of at least three layers: (1) a clear zone, outside the endothelial cell, referred to as the lamina rara interna; (2) the fused basal laminae of both the endothelial cell and the podocyte, called the lamina densa; and (3) another clear area adjacent to the podocyte known as the lamina rara externa. The slit diaphragms which attach one foot process to the adjacent process are easily seen at this magnification. Pe, podocyte foot process; BM, fused basal lamina of the endothelial cell and podocyte; RBC, red blood cell.

D9 TEM of portion of rat glomerulus showing localization of laminin within glomerular basement membrane. The electron-dense reaction product, illustrating the localization of laminin, is present throughout the full thickness of the glomerular basement membrane and mesangial matrix. Red blood cells within the capillary lumen stain intensely because of the pseudoperoxidatic activity of hemoglobin. GBM, glomerular basement membrane; Ep, epithelial cell, or podocyte; En, endothelial cell; Me, mesangial cell; MM, mesangial matrix; RBC, red blood cell.

E1 High-magnification TEM of glomerular filtration barrier. Compare the morphology of this frame with that seen in D8. Reaction product representing the localization of laminin is present within the lamina rara interna (Lri), the lamina densa (Ld), and the lamina rara externa (Lre) of the glomerular basement membrane. Reaction product for laminin is absent immediately beneath the epithelial slit diaphragms seen at the arrowheads. CL, capillary lumen; En, endothelium; Ep, epithelium, or podocyte; US, urinary space.

E2 TEM of glomerular filtration barrier in rat glomerulus. The electron-dense marker, cationized ferritin, has been used to localize heparan sulfate proteoglycan within the glomerular filtration barrier. The heparan sulfate proteoglycan can be seen within the lamina rara interna (LRI) and the lamina rara externa (LRE) (see arrows). US, urinary space; Ep, epithelial cell or podocyte; fp, foot process; LD, lamina densa; En, endothelial cell; Cap, capillary lumen.

E3 Diagram illustrating biochemical nature of glomerular filtration barrier. The epithelial cell, or podocyte, foot processes are seen at the top. The dense line at their outer surface represents the high density of sialic acid groupings in the membrane. A similar but somewhat less intense staining is also seen on the surface of the endothelial cells. Small black triangles representing heparan sulfate proteoglycan are shown within the lamina rara interna and the lamina rara externa. Laminin is present throughout the glomerular filtration barrier. Other components of the glomerular filtration barrier include fibronectin and type IV collagen within the lamina densa. Hyaluronic acid has been detected within the barrier as well. These agents play a key role in the function of the glomerular filtration barrier, since removal of the heparan sulfate proteoglycan, hyaluronic acid, or laminin can interfere with the morphology of the barrier and thus compromise the function of the barrier.

E4 Diagram of nephron depicting relationships of proximal tubule, loop of Henle, and distal tubule to renal corpuscle and collecting duct.

E5 LM of renal corpuscle illustrating vascular pole and opening of urinary pole into proximal convoluted tubule. (H & E)

E6 High-magnification LM of kidney cortex showing examples of proximal convoluted tubules in cross section and a portion of proximal straight tubule. (H & E)

E7 TEM of proximal convoluted tubule in kidney.

E8 High-magnification TEM of proximal convoluted tubule cell. Observe the extensive brush border, the large number of mitochondria, lysosomal bodies, and the extensive infolding of the lateral and basal membranes of the cell.

E9 SEM of proximal convoluted tubule cell in rat kidney. Note the extensive interdigitating folds of the lateral surface and basal surface of this cell.

F1 LM of medullary ray, with examples of collecting duct, proximal straight tubules, and ascending thick segment of loop of Henle. (H & E)

F2 TEM of proximal straight tubule at junction with thin segment, or descending limb, of loop of Henle. C, capillary; DH, descending limb of Henle; and DT, distant tubule.

F3 LM of medulla in kidney. A collecting duct, loop of Henle, capillaries, and ascending thick limb of the loop of Henle are easily seen. Also note the presence of interstitial cells within the connective tissue between adjacent tubules and capillaries. (H & E)

F4 TEM of loop of Henle showing transition between descending thin limb and ascending thin limb of loop of Henle. Interstitial cells lie between the two loops. CAP, capillary; INT, interstitum; DTL-1, descending thin limb; ATL, ascending thin limb.

F5 Diagram of countercurrent multiplier mechanism illustrating osmolarity and formation of urine within nephron.

F6 LM depicting immunocytochemical localization of ATPase within ascending thick limb of loop of Henle.

F7 TEM of ascending thick limb of loop of Henle in rat kidney.

F8 LM illustrating entrance of afferent arteriole into vascular pole of renal corpuscle in kidney. Note the macula densa (top). (H & E)

F9 LM illustrating immunocytochemical localization of renin within afferent arteriole entering vascular pole of renal corpuscle. Compare with 8.

G1 LM showing vascular pole of renal corpuscle and adjacent macula densa. (H & E)

G2 TEM of macula densa and adjacent JG cells associated with another afferent arteriole. The lumen of the distal tubule (macula densa) is at left. Em, extraglomerular mesangium; Ga, Golgi apparatus; GC, granule complex; and MD, macula densa.

G3 TEM of smooth muscle cells of afferent arteriole in juxtaglomerular apparatus. A portion of cells in the macula densa are visible (top). Large, irregular, and dense granules are present within the modified smooth muscle cells involved in the secretion of renin. Gr, granules.

G4 LM illustrating several proximal convoluted tubules as well as distal convoluted tubule (right). Notice the difference in the height of the epithelium and the presence of a microvillous border. (H & E)

G5 TEM of distal convoluted tubule. Observe the lack of a well-developed microvillous border and the presence of numerous mitochondria within folds in the basal cytoplasm.

G6 LM of collecting duct in medullary ray of kidney cortex. Observe the cell height and the diameter of the tubule lumen. (H & E)

G7 TEM of collecting duct in kidney. Note the absence of a well-developed microvillous border and the paucity of mitochondria, as compared with characteristics of distal tubule, ascending thick limb of the loop of Henle, or the proximal tubule.

G8 TEM of interstitial cells within kidney medulla. Observe a portion of a capillary (lower left) and part of a collecting duct (upper right). The interstitial cells are an important part of kidney function since they are involved in the production of prostaglandins. CD, collecting duct; IS, interstitial space; and LD, lipid droplet; arrow, cytoplasmic process of interstitial cell.

G9 SEM of renal papilla in kidney. The large collecting ducts that open onto the surface, or tip, of the papilla are called the ducts of Bellini. The surface of the papilla, pierced by many of these ducts, is referred to as the area cribrosa.

Acknowledgments

A1 Reproduced with permission from Sergei P. Sorokin, *Histology*, 4th edition, L. Weiss and R. O. Greep, editors, McGraw-Hill, New York, NY, 1977.

A9 Reproduced with permission from Marianne Bachofen, American Review of Respiratory Diseases, Vol. 3, American Lung Association, New York, NY, 1975.

B1 Reproduced with permission from L. Junqueira, *Basic Histology*, 4th edition, L. Junqueira and J. Carniero, editors, Lange Medical Publications, Los Altos, CA, 1980.

B2 Reproduced with permission from Tatsuo Ebe and S. Kobayashi, *Fine Structure of Human Cells and Tissues*, T. Ebe and S. Kobayashi, editors, Igaku-Shoin, Tokyo, Japan, 1972.

B3 Reproduced with permission from Lelio Orci, *Freeze Etch Histology*, L. Orci and A. Perrelet, editors, Springer-Verlag, New York, NY, 1975.

B6 Reproduced with permission from James O. Shaw, American Journal of Pathology 101:283, 1980.

B7 Reproduced with permission from Allen B. Cohen, Federation Proceedings 38:2635, 1979.

B8, B9 Reproduced with permission from D. Zucker-Franklin et al., *Atlas of Blood Cells*, Vol. 1, Edi Ermes s.r.l., Milano, Italy, 1981.

C9, D2 Courtesy of Dr. Masayuki Miyoshi, Department of Anatomy, Fukuoka University, School of Medicine, Fukuoka, Japan.

D3, D7 Courtesy of Dr. Franco Spinelli, Medical Research Department, Hoffman-LaRoche, Ltd., Basel, Switzerland.

D4 Reproduced with permission from Marilyn Farquhar, Kidney International 8:197, 1975.

D5 Reproduced with permission from Tsuneo Fujita, *SEM Atlas of Cells and Tissues*, T. Fujita, K. Tanaka, and J. Tokunaga, editors, Igaku-Shoin, Tokyo, Japan, 1981.

D6 Reproduced with permission from Junichi Tokunaga, Archivum Histologicum Japonicum 37:165-82, 1974.

D8, G3 Reproduced with permission from Ruth Bulger, *Histology*, 4th edition, L. Weiss and R. O. Greep, editors, McGraw-Hill, New York, NY, 1977.

D9, E1 Courtesy of Dr. Dale Abrahamson, Department of Anatomy, University of Alabama, Birmingham, AL.

E2, E3 Reproduced with permission from Marilyn Farquhar, Journal of Cell Biology 81:137, 1979.

E7, G7 Reproduced with permission from Arvid B. Maunsbach, *Electron Microscopy in Human Medicine*, Vol. 9, J. V. Johannessen, editor, McGraw-Hill, New York, NY, 1979.

E8, F7, E9, G5 Courtesy of Dr. Ruth Bulger, Department of Pathology and Laboratory Medicine, University of Texas Health Science Center, Houston, TX.

F2 Courtesy of Dr. Lydia Osvaldo, Karolinska Institutet, Stockholm, Sweden.

F4 Reproduced with permission from Melvin Schwartz, Kidney International 6:193, 1974.

F5 Reproduced with permission from L. Mary Pickford, *A Companion to Medical Studies*, Vol. 1, R. Passmore, editor, Blackwell Scientific Publications, Osney Mead, Oxford, England, 1968.

F6 Courtesy of Dr. Denis Baskin, Diabetes Research Center, University of Washington, Seattle, WA.

F9 Courtesy of Dr. Marco Celio, Department of Anatomy, University of Zurich, Zurich, Switzerland.

G2 Courtesy of Dr. Luciano Barajas, Department of Pathology, UCLA School of Medicine, Torrance, CA.

G8 Courtesy of Drs. Richard Majack and William Larson, Department of Anatomy, College of Medicine, University of Iowa, Iowa City, IA.

G9 Reproduced with permission from Mario Castelluci, *Three Dimensional Microanatomy of Cell and Tissue Surfaces*, D. J. Allen, P. M. Motta, and L. J. A. DiDio, editors, Elsevier, Amsterdam, Netherlands/New York, NY, 1981.

A1 LM showing wall of ureter. Transitional epithelium lines the slitlike, star-shaped lumen and overlies a thin lamina propria. The muscularis layer of the ureter consists of smooth muscle arranged in alternating longitudinal, circular, and longitudinal arrays. (H & E)

A2 Higher-magnification LM of ureter. It shows transitional epithelium, delicate connective tissue within the lamina propria, and alternating layers of smooth muscle in the muscularis. (H & E)

A3 Low-magnification LM of urinary bladder. Large bundles of smooth muscle are found within the thick wall of the bladder. These are usually arranged at oblique angles to one another, in sharp contrast to the well-organized circular and longitudinal arrays found within the gastrointestinal tract. (H & E)

A4 Higher-magnification LM of transitional epithelium lining urinary bladder. This tissue was fixed in the relaxed state, so that the large umbrella cells adjacent to the lumen can be seen overlying basal cells within the epithelium. (H & E)

A5 SEM of bladder showing luminal surface of umbrella cells.

A6 TEM of urinary bladder illustrating superficial layers of epithelial cells (umbrella cells). A portion of the lumen (marked L) is visible (upper right). Large numbers of discoid vesicles are present within the apical cytoplasm of the cell (see arrows). N, nucleus; M, mitochondria.

A7 High-magnification TEM of apical cytoplasm of umbrella cell, or superficial epithelial cell, in urinary bladder. Many disk-shaped vesicles are present within the apical cytoplasm and represent a form of membrane storage. Upon stimulation, these vesicles will fuse with the plasma membrane and thereby increase the surface area of the umbrella cell. dv, disk-shaped vesicles; M, mitochondria.

A8 TEM of urinary bladder showing apical surfaces of umbrella cells when stretched. Note the irregular surface of the cell created by the fusion of the disk-shaped vesicles with the apical cytoplasm. L, lysosomes; M, mitochondria; N, nucleus.

A9 SEM of luminal surface of umbrella cells in urinary bladder. Observe that the surface of the stretched epithelial cells now appears pockmarked as a result of the fusion of disk-shaped vesicles with the surface plasmalemma.

B1 Diagram of female reproductive tract.

B2 LM of ovarian cortex showing capsule, primordial follicles, several large secondary follicles, and stroma densely populated by spindle-shaped cells, a characteristic of the female reproductive tract.

B3 Macrophotograph of infundibulum, fallopian tube, ovary, and (at far right) body of uterus.

B4 LM of ovary. It shows many examples of primordial follicles and the transitional stage between primordial and primary follicle in which the formation of multiple layers of follicular cells has begun and a well-developed zona pellucida is present. (H & E)

B5 TEM of primordial follicle. The oocyte is surrounded by a single layer of closely apposed, flattened follicular cells. A basal lamina surrounds the primordial follicle and delineates it from the adjacent stroma of connective tissue located in the ovarian cortex. St, stroma; Bl, basal lamina; M, mitochondria; N, nucleus; G, Golgi, Oo, oocyte; n, nuclearlike body.

B6 TEM of developing primary follicle. Observe the zona pellucida between the oocyte surface and the surrounding follicular cells. Numerous follicular projections are evident within the zona pellucida, and some of these make junctional contacts with microvilli or the plasmalemma of the oocyte. The basal lamina subtends the follicular cells and separates them from the ovarian stroma. Concentric layers of cells within the stroma are beginning to from the theca. Ti, theca interna; Bl, basal lamina; Fc, follicular cells; Zp, zona pellucida; Oo, oocyte; N, nucleus; nu, nucleolus.

B7 LM of developing secondary follicle. Follicular cells now consist of multiple layers, and formation of an antrum has begun (on left). The stromal cells are now well organized into a theca interna and theca externa. (H & E)

B8 SEM of developing secondary follicle similar to that seen in B7. Observe the antrum, and the basal lamina which separates the follicular cells from the underlying stroma.

B9 Higher-magnification LM of secondary follicle seen in B7. Note the vascularity of the theca interna. The oocyte (lower right) is surrounded by a well-developed zona pellucida and adjacent granulosa cells. (H & E)

C1 High-magnification LM of oocyte in secondary follicle. The oocyte is surrounded by cumulus cells, which blend into the cumulus oophorus (left). A well-developed zona pellucida is present, and the nucleus and nucleolus are evident. (H & E)

C2 TEM of granulosa cells in cumulus-oocyte complex in large nonpreovulatory follicle from a rat. The innermost granulosa cells in the cumulus layer (corona radiata) send processes through the zona pellucida (ZP) to form contacts (gap junctions) with the plasma membrane of the oocyte (small arrows). Adjacent granulosa cells are also joined by gap junctions (large arrows).

C3 Dye coupling in three nonpreovulatory cumulus-oocyte complexes. In the top series of micrographs (A-D), the cumulus-oocyte complex was photographed with phase optics (A) and the dye fluorescein was injected. The dye rapidly spreads into adjacent granulosa cells after two minutes (Frame B), after nine minutes (C), and into more distant cells after 16 minutes (D). A second cumulus-oocyte complex is shown with phase optics (E), and dye transfer from the oocyte to the granulosa cells is shown after five minutes (F), 14 minutes (G), and 25 minutes (H). The cumulus-oocyte complex was photographed with phase optics in I, and then the oocyte was injected with fluorescein and subsequently photographed after 16 minutes (J), 48 minutes (K), and 51 minutes (L).

C4-C7 Series of four movie frames illustrating stages in ovulation. Shown in C4 is the initial rupture of the follicle. Illustrated in C5 is the expression of the liquor folliculi from within the antrum. In C6 the cumulus cells are being expressed from the follicle, and the egg can be seen as a small white ball just beyond the opening of the ruptured follicle. In C7 the entire cumulus mass has been expressed from the follicle. It is about to be picked up by the fimbriae of the infundibulum as they sweep over the surface of the ovary.

C8 Macrophotograph of section of ovary showing two large corpora lutea. One (on the right) can be considered a corpus hemorrhagicum since portions of the red cell clot can be seen within the lumen. The corpus luteum (on the left) is from a previous month's ovulation; it is undergoing regression and does not contain viable cells. (H & E)

C9 LM of corpus luteum. Large corpus luteal cells are visible (middle and right). Large vessels in the stroma surrounding the corpus luteum are sending small branches, accompanied by theca luteal cells, into the previously avascular corpus luteum. (H & E)

D1 Higher-magnification LM of corpus luteum showing theca luteal cells and large granulosa luteal cells. (H & E)

D2 TEM of granulosa luteal cell. These cells contain numerous mitochondria with tubular cristae and an abundant, smooth endoplasmic reticulum used in the production of steroid hormones. Small portions of rough endoplasmic reticulum are visible (lower right).

D3 LM of regressing corpus luteum. The ovarian stroma can be seen (right), and the luteal wall now consists of infiltrating mononuclear cells involved in the phagocytosis of degraded luteal cells. (H & E)

D4 TEM of regressing corpus luteum. Macrophages can be distinguished readily, by their numerous dense bodies, from luteal cells. Note that macrophages appear to be particularly abundant along the edge of the corpus luteum, a finding consistent with the symmetrical centripetal shrinkage that occurs as this structure involutes. Aging luteal cells contain numerous lipid droplets, many of which have been extracted by the solvents used during processing of the tissue for microscopy.

D5 TEM of regressing corpus luteum at higher magnification. Observe the large dense bodies and inclusions (right), which are remnants of degenerating luteal cells present within the cytoplasmic matrix of a macrophage. Aging luteal cells containing dense bodies are seen surrounding the macrophage.

D6 LM of corpus albicans in ovary. At the end of luteal lysis all that remains of the corpus luteum is the small scar consisting of collagen fibers, macrophages, a few fibroblasts, and occasionally some cells that bear a superficial resemblance to luteal cells. (H & E)

D7 Diagram of ovarian and uterine cycles. It shows the cyclic changes that occur in the ovary and in the uterine epithelium.

D8 Macrophotographs of ovaries. In the ovary from a three-year- old girl (left), note the fallopian tube and its flowerlike, funnel-shaped infundibular end. In the ovary from a 14-year-old girl (right), the uterine tube is somewhat longer, and the infundibulum is ready to move toward a follicle that is ready to rupture, to pick up the oocyte. Notice the scarred surface of the ovary, indicating previous ovulation.

D9 Macrophotograph showing relationship of oocyte to infundibulum after ovulation. During ovulation the fimbria forming the fringe around the end of the infundibulum fill with blood and are activated for picking up the oocyte. Movement or transport of the oocyte on the fimbria is dependent upon the presence of an intact cumulus layer around the oocyte.

E1 Macrophotograph of infundibular region during ovulation. It shows an oocyte and cumulus cells (stained blue) during transport toward the ostium of the uterine tube. The loss or lack of cumulus cells surrounding the oocyte at this particular time will prevent the oocyte from moving into the uterine tube.

E2 Macrophotograph of uterine tube revealing presence of stained oocyte in cumulus cells within lumen. Note the contraction band (upper left) illustrating the peristaltic movement of the tube involved in transport of the egg to the site of fertilization.

E3 LM of wall of uterine tube. Mucosal folds project into the lumen, which contains red blood cells as a result of hemorrhage at the time of surgery. (H & E)

E4 Higher-magnification LM of uterine tube. The epithelial lining of the uterine tube consists of simple columnar ciliated cells. (H & E)

E5 TEM of uterine tube showing ciliated cells within epithelial wall.

E6 SEM of surface of uterine tube epithelium illustrating paucity of ciliated cells during early follicular stage of ovarian cycle.

E7 SEM of surface of uterine tube epithelium displaying abundance of ciliated cells at mid-cycle.

E8 High-magnification SEM of uterine tube epithelium showing presence of spermatozoa on epithelial surface. Compare the structure of microvilli, cilia, and flagella. Fl, flagellum; MP, midpiece.

E9 SEM of oocyte and attached spermatozoon. In mammals, the spermatozoon fuses by its lateral surface with microvilli on the surface of the egg. See F1.

F1 SEM of the same spermatozoon on surface of oocyte as shown in E9. Note that the process of fusion of the spermatozoon membrane has already begun and that the lateral surface of the spermatozoon head has fused with the surface of the egg plasmalemma.

F2 LM of uterine endometrium during menstrual phase of uterine cycle. The uterine surface is still partially denuded of epithelium. Note the straight glands extending through the endometrium. (H & E)

F3 SEM of surface of uterus during menstrual phase of uterine cycle. In the low-magnification SEM of the uterine surface (left), several openings of tubular uterine glands can be seen. At higher magnification (right) an individual gland shows the epithelium as it migrates from the gland and recovers the surface of the uterus.

F4 LM of uterine endometrium during proliferative phase of uterine cycle. Observe the increased thickness of the endometrium and the coiling of the glands. The basalis region of the endometrium can be distinguished (far left). (H & E)

F5 SEM of uterine surface during proliferative phase of uterine cycle. Reepithelialization of the surface has been completed, and small numbers of ciliated cells are now beginning to appear. Several gland openings are seen in the low-magnification SEM (left); single gland opening is shown at higher magnification (right).

F6 LM of uterine endometrium during secretory phase of uterine cycle. Note the edematous accumulation of fluid within the endometrium and the high degree of coiling of uterine glands. An increased cellularity can also be seen within the lamina propria of the endometrium. (H & E)

F7 SEM of surface of uterine epithelium during secretory phase of uterine cycle. Signs of secretory activity can be seen (left) in a mucuslike discharge occurring within the openings of the uterine glands. At high magnification (right), large numbers of ciliated cells are present.

F8 LM of endometrium showing opening of a single uterine gland. The uterine surface is lined by a simple columnar ciliated epithelium. In the secretory phase of the uterine cycle, larger numbers of mononuclear cells infiltrate the lamina propria beneath the epithelium. (H & E)

F9 TEM of uterine epithelium including several nonciliated uterine epithelial cells. Note the simple columnar arrangement of the epithelium. Deposits of glycogen can be seen at large arrow, mitochondria at small arrow.

G1 Low-magnification LM of vagina. Unlike the GI tract, the vagina does not show any muscularis mucosa, nor are mucous glands present within the submucosa. Many smooth muscle bundles are present; however, there is no apparent organization into well-defined layers. (H & E)

G2 Higher-magnification LM of vaginal epithelium, which consists of stratified squamous, nonkeratinized cells. A lymphocytic infiltration can be seen in the lamina propria immediately beneath the epithelium. The underlying connective tissue is of a loose fibroelastic nature. (H & E)

G3 LM of mammary gland. The secretory acini are of variable size and contain a heterogeneous mottled secretory product in the lumen. Large ducts surrounded by connective tissue are also present. (H & E)

G4 Higher-magnification LM of secretory acini in mammary gland. Observe the irregular appearance of the secretory product within the lumen and the branching of the acini and ducts. (H & E)

G5 TEM of epithelium lining an alveolus in lactating mammary gland. Two large lipid droplets are present within the apical cytoplasm of the cells. Eventually the lipid droplets will be released into the lumen, where casein protein droplets are evident. At the base of the epithelium, a myoepithelial cell process can be seen, and in the lamina propria a continuous capillary containing an erythrocyte is present. C, casein; LD, lipid droplets; MV, myoepithelial cell process; RBC, red blood cell.

G6-G9 Blank

Acknowledgments

A5, A9 Reproduced with permission from Myron Tannenbaum, *Electron Microscopy* in Human Medicine, Vol. 9, J. V. Johannessen, editor, McGraw-Hill, New York, NY, 1979.

A6, A7, A8 Reproduced with permission from Keith Porter, Protoplasma 63:262, 1967.

B3, D8, D9 Reproduced with permission from Lennart Nilsson, *Behold Man*, Little, Brown, Boston, MA, 1973.

B5, B6 Courtesy of Dr. Jonathan Van Blerkom, Department of Molecular, Cellular, and Developmental Biology, University of Colorado, Boulder, CO.

B8 Courtesy of Dr. P. Bagavandoss, Department of Anatomy, University of Michigan, Ann Arbor, MI.

C2, C3 Reproduced with permission from Norton B. Gilula, Journal of Cell Biology 78:58, 1978.

C4-C7, E1, E2 Courtesy of Dr. Richard Blandau, Department of Biological Structure, University of Washington School of Medicine, Seattle, WA; from his film *Ovulation and Egg Transport in Mammals*, 1973.

D2 Courtesy of Dr. Arthur T. Hertig, New England Regional Primate Research Center, Southborough, MA.

D4, D5 Courtesy of Dr. Laurie G. Paavola, Department of Anatomy, Temple University School of Medicine, Philadelphia, PA.

E5 Courtesy of Dr. Ellen R. Dirksen, Department of Anatomy, University of California School of Medicine, Los Angeles, CA.

E6, E7 Courtesy of Dr. E. M. Eddy, Laboratory of Reproductive and Developmental Toxicology, National Institute of Environmental Health Sciences, National Institutes of Health, Research Triangle Park, NC.

E8 Reproduced with permission from Pietro M. Motta, Atlante di microscopia elettronica a scansione, Piccin Nuova Libraria S.p.A., Padova, Italy.

E9, F1 Reproduced with permission from David Phillips, *The Cell*, 2d edition, D. W. Fawcett, editor, Saunders, Philadelphia, PA, 1981.

F3, F5, F7 Courtesy of Dr. Hans Ludwig, University of Essen, Essen, Germany.

F9 Courtesy of Dr. Alex Ferenczy, McGill University, Montreal, Canada.

G5 Courtesy of Dr. Judy Strum, Department of Anatomy, University of Maryland School of Medicine, Baltimore, MD.

A1 Diagram illustrating organization of testis, accessory male reproductive organs, and penis.

A2 Macrophotograph of testis showing excision of tunica albuginea and underlying seminiferous tubules.

A3 LM of tunica albuginea and overlying epithelium in testis. Observe the thick collagenous nature of this capsulelike stroma. (H & E)

A4 Macrophotograph showing nature of seminiferous tubules. The tunica albuginea has been removed. Compare with A2.

A5 SEM of seminiferous tubules as revealed by fracture of testis. Small amounts of connective tissue can be seen around the periphery of each tubule. Within the tubule are examples of various stages of spermiogenesis.

A6 LM of seminiferous tubules in testis. Each seminiferous tubule is surrounded by a layer of myoid cells. The epithelium consists of Sertoli cells and germinative cells in various stages of development. Between the tubules can be seen blood vessels, lymphatics, and clusters of Leydig cells (which are acidophilic). (H & E)

A7 LM of seminiferous tubules after intravascular injection of horseradish peroxidase. The dense reaction product for the peroxidase enzyme is present within the interstitial tissue and surrounds the seminiferous tubules. No peroxidase can be found within the lumen of the seminiferous tubules, suggesting the presence of a blood testis barrier.

A8 Higher-magnification LM of seminiferous tubule epithelium. Myoid cells surround the seminiferous epithelium. Spermatogonia are seen at the periphery of the epithelium, whereas the Sertoli cell nuclei appear vesicular, contain a prominent nucleolus, and are removed from the basement membrane by one or two nuclei of spermatogonia. Above the Sertoli cell nuclei are spermatocytes in various stages of spermatogenesis. Spermatids border the lumen. (H & E)

A9 Blank

B1 High-magnification LM of epithelium of seminiferous tubule. Note the myoid cell layer at the base of the epithelium, the spermatogonia, Sertoli cells, various stages of developing spermatocytes, and spermatids embedded within the apical cytoplasm of Sertoli cells. (H & E)

B2 Diagram of various stages in spermatogenesis and spermiogenesis. Observe the division of chromosomes during meiosis (left).

B3 LM demonstrating immunocytochemical localization of the enzyme aldose reductase within cytoplasm of Sertoli cells. Observe the tall, columnar nature of the Sertoli cell (in left tubule) as it extends from the basement membrane to the lumen. The spermatids (in tubules at lower right) are embedded within the positive-staining cytoplasm of the Sertoli cell.

B4 TEM of Sertoli cell showing relationships of developing spermatids to Sertoli cell cytoplasm and late-developing spermatids embedded in apical surface.

B5 TEM of basal portion of Sertoli cell from a primate. Large numbers of filaments (indicated by arrowheads) surround the nucleus. Also present within the cytoplasm are large amounts of smooth, or agranular, endoplasmic reticulum and lipid droplets.

B6 LM of isolated Sertoli cell. Note its luminal surface (left) and developing spermatids embedded in its apical cytoplasm.

B7 LM of cross and longitudinal sections of seminiferous tubule (left) and diagrams of the six stages in spermatogenesis seen in the human (right). These six stages of development are not arranged sequentially within a single tubule but are interspersed as patches of development as shown in the cross and longitudinal sections.

B8 Fluorescent LM of seminiferous tubule stained with acridine orange. Note the variation in staining of nuclear chromatin during the stages of spermatogenesis. Myoid cells, spermatogonia, primary and secondary spermatocytes, as well as spermatids can be seen.

B9 TEM of spermatogonia in seminiferous tubule after intravenous injection of horseradish peroxidase. Reaction product for the peroxidase enzyme has penetrated between the cells and completely surrounds the spermatogonia. The spermatogonium is found within the basal compartment, whereas more mature spermatocytes and spermatids lie within the adluminal compartment.

C1 TEM of spermatogonium in seminiferous tubule from a primate. The outline of the cell is defined by the electron-dense tracer lanthanum nitrate. The presence of junctional complexes between adjacent Sertoli cells (shown by arrowheads) above the spermatogonium prevents the electron-opaque tracer from penetrating deeper into the seminiferous epithelium. Thus, circulating plasma proteins are excluded from the luminal or adluminal compartment of the seminiferous tubule, and it is likely that the Sertoli-Sertoli junctional complexes are the morphological site of this barrier.

C2 TEM of spermatogonia in seminiferous epithelium. Note the presence of cellular bridges between spermatogonia that have recently divided.

C3 TEM of developing spermatids within seminiferous epithelium. Note the accumulation of electron-dense material within the acrosomal cap in the spermatids and the presence of intercellular bridges.

C4 Diagram of various stages in spermiogenesis in the human.

C5 TEM of spermatids in primate testis showing changes in nuclear condensation and acrosome formation. A cap phase spermatid is illustrated (left), with arrowheads indicating the acrosomal cap. A spermatid in the acrosomal phase is observed (center); note the intimate association of smooth endoplasmic reticulum (arrowheads) with the spermatid tail. Also shown is a spermatid in the maturation phase (right). Compare the condensation of nuclear chromatin in all three stages, as well as the shape of the acrosome. All these stages occur while these spermatids reside within deep invaginations of the Sertoli cell surface. G, acrosomal granule; SER, smooth endoplasmic reticulum.

C6 High-magnification TEM of developing spermatids embedded in invaginations of Sertoli cell. Note the stalk connecting the residual cytoplasm to the developing spermatid. Eventually the residual cytoplasm will be engulfed, phagocytosed, and degraded by the Sertoli cell.

C7 Diagram of structure of spermatozoon.

C8 Phase LM of spermatozoa showing flattened heads of spermatozoa in different planes. Observe the small amount of residual cytoplasm in the mid-piece region of one spermatozoon (center).

C9 SEM of spermatozoa. The extent of the acrosome and the postacrosomal segment of the sperm head is evident. Note that the sperm heads have a typical ovoid profile, while little surface detail is seen in the flagellum. A, acrosomal cap; PA, postacrosomal segment; F, flagellum.

D1 Composite TEMs of spermatozoa.

In panel A the plane of section of the head of the spermatozoon is perpendicular to the plane of view shown in Frame C9. Note the tapering of the sperm head. The acrosome is finely granular, with a homogeneous matrix. The plasmalemma is fairly loose-fitting over the acrosome but closely applied over the postnuclear sheath. The plasmalemma loses its close association with the nucleus at the posterior ring. The nucleus is a highly condensed mass of granular chromatin.

Panel B shows a longitudinal section of connecting piece and mid-piece of sperm flagellum. The segmented columns of the connecting piece fuse to the outer dense fibers. The proximal centriole is positioned in the connecting piece and is shown in transverse section. The mitochondria are placed circumferentially around the outer dense fibers. At the termination of the mid-piece, the annulus is visible as an electron-dense zone associated with the plasma membrane. The ribs of the fiber sheath are shown in grazing section.

Panel C is a cross section through the distal region of the connecting piece. The mitochondrial sheath is present, as are the segmented columns of the outer dense fibers. In the axoneme, the central pair of microtubules is lacking at this point in the flagellum.

Panel D illustrates a cross section of the mid-piece region of the flagellum and demonstrates mitochondria and outer dense fibers.

Panel E is a cross section of the proximal end of the principal piece of the flagellum. The fiber sheath is represented in cross section by the ribs and continuous columns.

Panel F shows a section through the distal end of the principal-piece region of the flagellum. The outer dense fibers have terminated, and the fibrous sheath is now much thinner and surrounds the nine plus two axonemal profile in the flagellum.

Panel G shows a cross section through the end piece of the flagellum containing only the nine plus two microtubules in the axoneme.

Panel H is a cross section through the distal segment of the end piece. The nine plus two axonemal geometry is lost, and some microtubules are incomplete.

Abbreviations for panels A and B: A, acrosome; PM, plasma membrane; PNS, postnuclear sheath; PR, posterior ring; N, nucleus; CP, connecting piece; ODF, outer dense fibers; PC, proximal centriole; M, mitochondria; A, annulus; R, ribs.

Abbreviations for panels C through H: CP, segmented columns; M, mitochondrial sheath; Mt, microtubules; ODF, outer dense fibers; C, columns; R, ribs.

D2 LM of interstitial space between seminiferous tubules in testis. The acidophilic Leydig cells are present in this space, together with vessels and lymphatics. (H & E)

D3 TEM of interstitial space between seminiferous tubules showing close association between Leydig cells and blood vessels. Leydig cells also appear to be directly exposed to lymph in lymphatic sinusoids.

D4 Higher-magnification TEM of Leydig cells revealing presence of crystals of Reinke within cytoplasm of Leydig cell.

D5 Diagram illustrating hormonal relationships between pituitary gland, Leydig cell, and Sertoli cell. E estradiol; T, testosterone; LH, luteinizing hormone; and FSH, follicle-stimulating hormone.

D6 LM of testis showing transition from seminiferous tubules to short tubuli recti. The latter open into a network of epithelial-lined channels, called the rete testis, which lie in the mediastinum of the testis. See A1. (H & E)

D7 TEM of lining epithelium in rete testis of a primate. Notice the presence of flagella within the apical cytoplasm. Testicular fluid and spermatozoa which are nonmotile at this point are transported from the rete testis to the ductus epididymis.

D8 LM showing transition between rete testis and ductuli efferentes. (H & E)

D9 TEM of epithelium of ductuli efferentes in a 33-year-old man. Ciliated and nonciliated cells are hard to distinguish. In the apical cytoplasm of nonciliated cells, many secretory granules can be seen. Numerous lysosomes are also present within these cells.

E1 LM of tubules in epididymis. The epithelium is pseudostratified columnar, rests on a basal lamina, and is surrounded by smooth muscle fibers arranged in circular fashion. Spermatozoa can be seen within the lumen of the tubules. (H & E)

E2 Higher-magnification LM of pseudostratified columnar epithelium of epididymis. The luminal surface of the epithelium bears long, nonmotile microvilli called stereocilia. Small, round cells containing spherical nuclei are seen at the base of the epididymal epithelium. (H & E)

E3 TEM of pseudostratified columnar epithelium of ductus epididymis. Rounded basal cells and columnar principal cells are visible. The supranuclear cytoplasm has many electron-dense vesicles, multivesicular bodies, and lysosomes. Stereocilia emanate from the apical surface of the cells.

E4 LM of ductus deferens in cross section. The mucosa protrudes into the lumen in several low folds. The structure of the epithelium in the ductus deferens is similar to that seen in the epididymis, but epithelial cells are not as tall. Surrounding the mucosa of the vas deferens are three layers of smooth muscle cells. The fibers of the inner and outer layers are arranged longitudinally; those of the middle layer, circularly. (H & E)

E5 Higher-magnification LM of mucosal surface within ductus deferens. The epithelium is pseudostratified columnar and contains stereocilia projecting from the apical cytoplasm. Frequently the stereocilia are matted together and form conelike structures, as seen in this frame. (H & E)

E6 Macrophotograph of seminal vesicle (left) and ampulary region of ductus deferens (right). The ductus deferens contains a highly branched mucosa resembling that seen within the seminal vesicle. (H & E)

E7 LM of seminal vesicle illustrating branching and anastomosing of secondary and tertiary folds of mucosa which join to form numerous irregular channels within the lumen of the gland. The lamina propria contains many elastic fibers, and smooth muscle cells course through the connective tissue. (H & E)

E8 LM of secretory epithelium within seminal vesicle. This epithelium may consist of either a simple columnar or a pseudostratified columnar epithelium.

E9 TEM of simple columnar epithelium in seminal vesicle. The secretory cells contain a single oval-shaped nucleus and, within the apical cytoplasm, numerous electron-lucent granules. Lysosomes are also obvious within the Golgi region. L, lumen; G, granules; LY, lysosomes; N, nucleus; ER, rough endoplasmic reticulum.

F1 LM of prostate gland. The mucosa of the gland forms a series of folds, and concretion granules are present within the lumen. Lamina propria consists of a fibromuscular stroma. (H & E)

F2 Higher-magnification LM of prostatic alveoli showing large concretion granules within lumens. The epithelium is normally either simple columnar or pseudostratified columnar. (H & E)

F3 LM of prostate gland processed immunocytochemically for detection of acid phosphatase. The presence of this enzyme is a reliable and sensitive test for assessing prostatic function and, as seen in this frame, is found only within the prostatic epithelium.

F4 TEM of simple columnar epithelium in prostate gland. These secretory epithelial cells possess luminal microvilli and an abundance of rough endoplasmic reticulum. Many secretory granules are present within the cytoplasm of these cells. The size and height of this epithelium are dependent upon the presence of testosterone.

F5 Macrophotograph of penis in cross section. Note the incomplete septum dividing the corpora cavernosa, and observe the urethra within the corpus spongiosum. A dense fibrolastic connective tissue layer, the tunica albuginea, binds the three cavernous bodies and also provides an attachment to the skin overlying the shaft of the penis. (H & E)

F6 Higher-magnification LM of corpus spongiosum showing location of penile urethra. Portions of seromucous glands and small ducts are seen in the lower part of the field.

F7-F9 Blank

G1-G9 Blank

Acknowledgments

A2, A4, B6, B8 Courtesy of Dr. Richard Blandau, Department of Biological Structure, University of Washington School of Medicine, Seattle, WA; from his film *Sperm Maturation in the Male Reproductive Tract: Development of Motility*, 1968.

A5 Courtesy of Dr. A. Kent Christensen, Department of Anatomy, University of Michigan School of Medicine, Ann Arbor, MI.

A7, B5, B9, C1 Reproduced with permission from Martin Dym, Anatomical Record 175:639, 1973.

B3 Courtesy of Dr. Mark Ludvigson, U.S. Army Medical Corps, St. Paul, MN.

B4 Reproduced with permission from D. W. Fawcett, *Handbook of Physiology*, Section 7, Vol. 5, *Male Reproductive Tract*, D. W. Hamilton and R. O. Greep, editors, American Physiological Society, Bethesda, MD, 1975.

B7 Reproduced with permission from Yves Clermont, American Journal of Anatomy 112:35, 1963.

B8 Courtesy of Dr. D. Szabo, Institute of Experimental Medicine, Hungarian Academy of Sciences, Budapest, Hungary.

C2 Reproduced with permission from Martin Dym and D. W. Fawcett, Biology of Reproduction 4:195, 1971.

C3 Reproduced with permission from Donald W. Fawcett, A *Textbook of Histology*, 10th edition, W. Bloom and D. W. Fawcett, editors, Saunders, Philadelphia, PA, 1975.

C4 Reproduced with permission from D. W. Fawcett, W. A. Anderson, and D. M. Phillips, Developmental Biology 26: 220, 1971.

C5 Reproduced with permission from Martin Dym, *Basic Reproductive Medicine*, Vol. 2, D. W. Hamilton and F. Naftolin, editors, MIT Press, Cambridge, MA, 1982.

C6 Reproduced with permission from D. W. Fawcett, Journal of Reproduction and Fertility, Supplement 6, 1969.

C7 Reproduced with permission from Histology, 4th edition, L. Weiss and R. O. Greep, editors, McGraw-Hill, New York, NY, 1977.

C9, D1 Reproduced with permission from Gary Olson, *Basic Reproductive Medicine*, Vol. 2, D. W. Hamilton and F. Naftolin, editors, MIT Press, Cambridge, MA, 1982.

D3 From the collection of Dr. R. Vitale, whom we have been unable to locate to obtain his permission.

D4 From the collection of Dr. David W. Hamilton, Department of Anatomy, Medical School, University of Minnesota, Minneapolis, MN. We have been unable to identify the original source.

D5 Courtesy of Dr. David W. Hamilton, Department of Anatomy, Medical School, University of Minnesota, Minneapolis, MN.

D7 Reproduced with permission from Martin Dym, Anatomical Record 186:514, 1976.

D9, E3 Courtesy of Dr. A. F. Holstein, Department of Microscopical Anatomy, University of Hamburg, Hamburg, West Germany.

E9 Reproduced with permission from L. F. Cavazos, *Handbook of Physiology*, Section 7, Vol. 5, D. W. Hamilton and R. O. Greep, editors, American Physiological Society, Bethesda, MD, 1975.

F3 Courtesy of Drs. Clive Taylor and W. Y. Naritoku, Department of Pathology, University of Southern California, Los Angeles, CA.

F4 Reproduced with permission from F. Gyorkey and P. Gyorkey, *Male Accessory Sex Glands*, E. Spring-Mills and E. S. E. Hafez, editors, Elsevier, Amsterdam, Netherlands/New York, NY, 1980

Index

Following is a key to abbreviations used in the index:

D	diagram	SEM	scanning electron micrograph
FF	freeze-fracture	T	table
LM	light micrograph	TEM	transmission electron micrograph
M	macrophotograph		

Boldface capital F precedes fiche number

This page intentionally left blank

Stanley L. Erlandsen earned his doctorate in anatomy at the University of Minnesota in 1967, and was a postdoctoral fellow at the University of Washington. He has taught at the University of Iowa and, since 1974, in the Medical School at the University of Minnesota, where he is now professor of anatomy. Erlandsen is co-author of *Giardia and Giardiasis: Biology, Pathogenesis and Epidemiology* (1984) and serves on the editorial boards of *The Journal of Histochemistry and Cytochemistry* and *The Anatomical Record*.

Jean E. Magney earned a B.S. in occupational therapy and an M.S. in anatomy at the University of Minnesota. She was an instructor and illustrator in the department of physical medicine and rehabilitation at Minnesota from 1971 until 1980, and since 1979 has been an instructor in the department of anatomy, University of Minnesota Medical School. Magney is co-author and illustrator of *Care of the Disabled Urinary Tract* (now in press).